International Union of Geodesy and Geophysics

International Association of Geodesy

2015-2019

Korean National Report to IAG

National Report to the XXVII General Assembly

Montreal, Canada

8. – 18. July, 2019.

Edited by

Jungho Cho

National Delegate of IAG Council,

Korea Astronomy & Space Science Institute (KASI)

Contributions from Sang-Oh Yi (National Geographic Information Institute: NGII), So-Young Park (NGII), Hyun-Ho Kim (NGII), Seung-Weon Shin (NGII), Kyoung-Min Roh (KASI), and Mansoo Choi (KASI)

CONTENTS

Korean National Report to the International Association for Geodesy, 2019

1. INTRODUCTION

Over the period from 2015 to 2019, meaningful progresses on Space Geodesy in South Korea have been made. On the aspect of Global Geodetic Observing System (GGOS) of International Association of Geodesy (IAG), National Geographic Information Institute (NGII) and Korea Astronomy and Space Science Institute (KASI) has successfully cooperated to establish the Sejong geodetic fundamental site in which GNSS, VLBI, and SLR are collocated since 2015. As needs of real time GNSS data both in geodetic and public are growing, a GNSS data sharing system was opened in 2016 as a real time web-service in which 174 GNSS sites nation-widely distributed are available.

KASI has taken the role of GPS Radio Occultation (RO) data center under the collaboration with University Corporation for Atmospheric Research (UCAR), National Oceanic and Atmospheric Administration (NOAA), Korea Meteorological Administration (KMA), and Korea Aerospace Research Institute (KARI) since 2014. During the period, researches on natural hazards monitoring and Earth rotation modelling had been performed at KASI while NGII mainly focused on strengthening the role of geodetic VLBI facility as the national geodetic origin and improving the national geoid model KNGeoid18. In recent years, Korea Positioning System (KPS) designed to be seven satellites is under preliminary study regarding reference frame, time system, and signal structure. This idea will be in depth investigated for the feasibility and the usefulness by government.

Korean GNSS Network (KGN), which consists of Continuously Observing Reference Station (CORS), has been upgraded by changing the GNSS receiving system and related facilities in last few years. NGII cooperates with eight domestic institutions to make the GNSS Data sharing platform in order to provide unified GNSS CORS data service. KASI has been operating a data center of GPS radio occultation data obtained from the Atmosphere Occultation and Precision Orbit Determination (AOPOD) system onboard Korea Multi-Purpose Satellite (KOMPSAT)-5 since 2013. KOMPSAT-5 radio occultation products are now available to worldwide weather communities via Global Telecommunication System of the World Meteorological Organization (WMO) information system.

KASI completed the construction of the Accurate Ranging system for Geodetic Observation

(ARGO) which consists of a mobile and a fixed SLR system. The ARGO-M (40 cm mobile SLR) was developed in 2012 and relocated to Sejong GGOS site from KASI Headquarter, Daejeon in July 2015 and the ARGO-F (1 m fixed SLR) was established with adaptive optics at Geochang site in November 2017. The ARGO-M and the nearby VLBI and GNSS stations of NGII will be fiducial stations for the International Terrestrial Reference Frame (ITRF). Since September 2014, the geodetic VLBI system of NGII has been a participant of the geodetic observation program of the IVS, an international body for VLBI. From the second quarter of 2019, local tie survey will be started by integrating the various space geodetic observation stations in Sejong.

NGII maintains the gravity control point which consists of absolute and relative gravity points. In the course of this duty, NGII has developed Korea National Geoid (KNGeoid) model since 2009 in order to provide the optimal precise geoid over whole Korean peninsula. The latest version is the KNGeoid18 with a higher precision and a wider range. Meanwhile, research works on Earth Orientation Parameters (EOP) Analysis based on a Machine Learning Algorithm, Loading Effects on Reference Frame, and GNSS meteorological applications have also been actively done and several key results are summarized in this report.

2. SPACE GEODETIC INFRASTRUCTURE

2.1 GNSS

For the GNSS-based geodetic surveying and an establishment of a positional reference system, NGII operates the GNSS CORS distributed with approximately 40 km interspace and a master control center as shown in Figure 2-1. The first of these is the Suwon CORS, established in 1995. The CORS consists of GNSS receiver/antenna, dedicated communication lines, power management systems, and meteorological monitoring equipment for temperature and humidity, etc. The master control center comprises several components such as a real-time monitoring system of the CORS status, a real-time data calibration service (Networked Transport of RTCM via Internet Protocol: NTRIP) system, a GNSS data sharing system, and a precise positioning and displacement monitoring system.
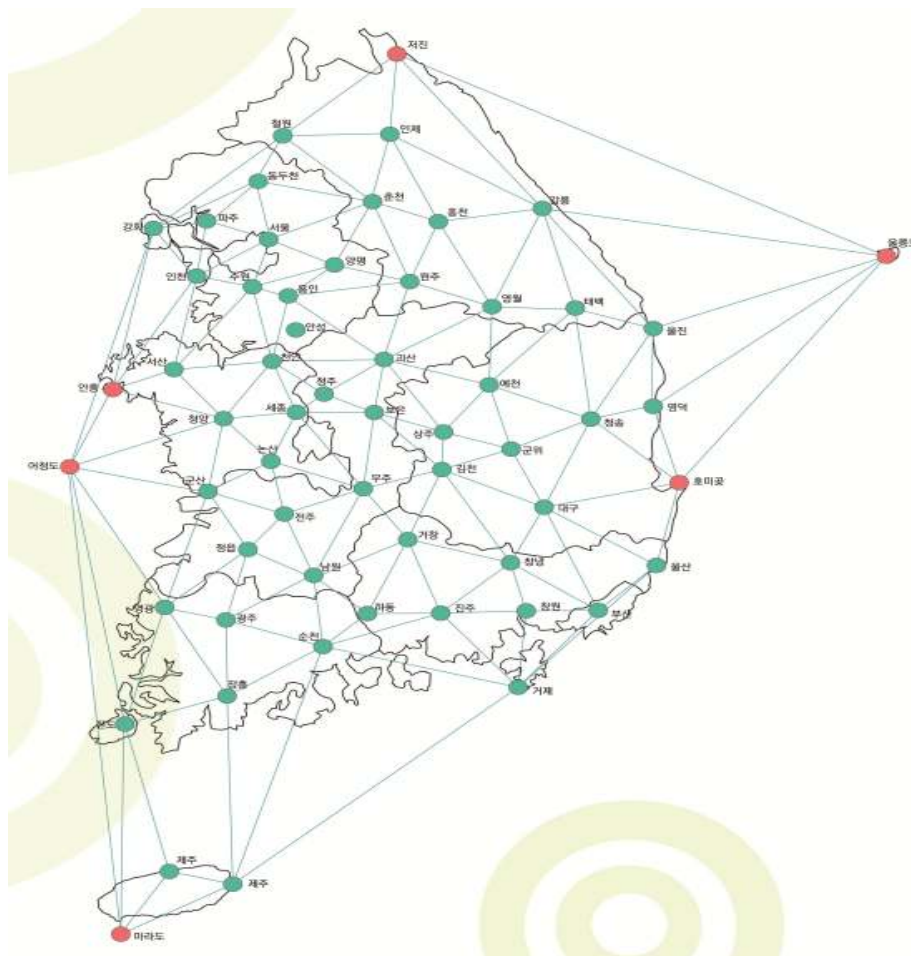

Figure 2-1. NGII GNSS CORS

Figure 2-2. NGII GNSS CORS at Uljin

The CORS has Trimble or Leica equipment for continuous observation of satellite signals such as GPS, GLONASS, Galileo and Beidou. Data observed at CORS are collected in real-time at the NGII GNSS master control center. The center monitors CORS and provides the observation data with RINEX format to support precise positioning and various real-time calibration data services.

KASI is operating 11 GNSS reference stations including one IGS station DAEJ. Two of these stations are located in the Chuuk Island of Micronesia (CHUK) and the Sainshand of Mongolia (SSND). The geographical location of the reference stations is shown in Fig. 2-3.
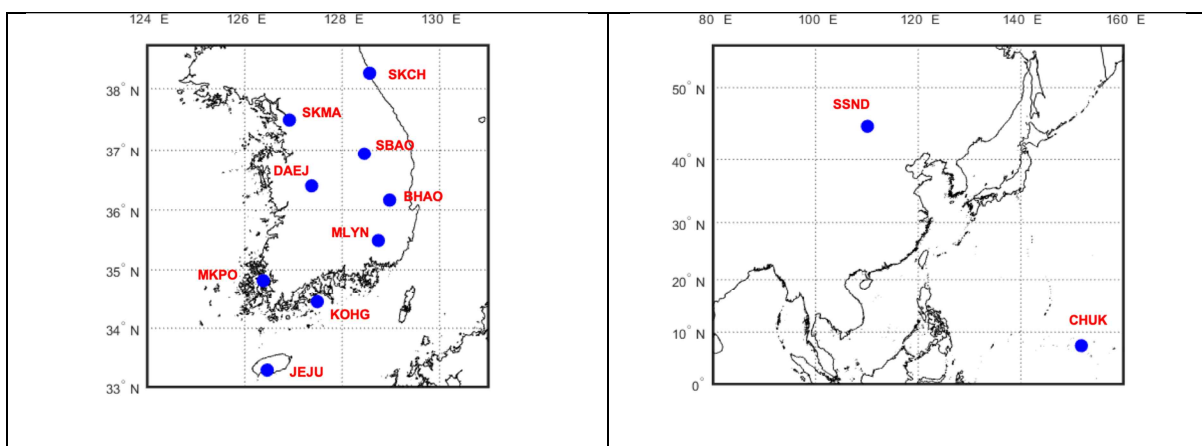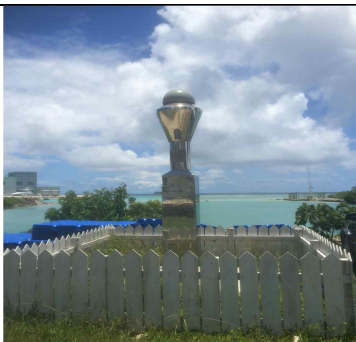

Figure 2-3. KASI GNSS CORS

In 2017, KASI has replaced the SCIS type radome as shown in Fig. 2-4.

SKMA	SKCH
MKPO	MLYN
BHAO	KOHG
JEJU	SBAO
SSND	CHUK

Figure 2-4. Image of the KASINET GNSS stations

KASI is also operating the IGS global data center (GDC) that archives and provides GNSS data from the Asia-Oceania region. The KASI GDC also archives and shares all the IGS products from worldwide IGS stations and IGS analysis centers (ftp://nfs.kasi.re.kr, http://gdc.kasi.re.kr). In 2018, KASI extended GDC storage by adding another 32TB real-time backup disk to prevent from a disk failure.

In addition, KASI has been operating a monitoring station (DAE2) of the Japanese Quasi-Zenith Satellite System (QZSS) signals since 2011. In international collaboration with the French space agency (CNES) and Institute Geographique National (IGN), KASI has been established REGINA (REceiver GNSS network for IGS and NAvigation) in South Korea for scientific purposes regarding the GNSS positioning and navigation. The REGINA GNSS station (GAMG) began regular operation in July 2016 and was registered in 2018 as an IGS network.

As a spaceborne GNSS infrastructure, KASI has been operating a data center of GPS radio occultation data obtained from the Atmosphere Occultation and Precision Orbit Determination (AOPOD) system onboard Korea Multi-Purpose Satellite (KOMPSAT)-5 since 2013 in collaboration with University Corporation for Atmospheric Research COSMIC Data Analysis and Archive Center (CDAAC) for data processing and distribution to research community. In order to make the data available in near real-time for numerical weather prediction, KASI is working with Korea Aerospace Research Institute (KARI) and National Oceanic and Atmospheric Administration (NOAA) National Environmental Satellite Data, and Information Service to increase downlink capability reducing the data latency. KOMPSAT-5 radio occultation products are now available to worldwide weather communities via Global Telecommunication System of the WMO information system; a global network of high-quality meteorological data distribution. Data and products are also available at AOPOD website (https://aopodweb.kasi.re.kr; ftp://aopod-ftp.kasi.re.kr) and CDAAC.

2.2 VLBI

Construction of the geodetic VLBI system, operated by the Space Geodetic Observation Center of NGII, was completed in June 2012 (Figure 2-5). Since September 2014, the system has been a participant of the geodetic observation program of the IVS, an international body for VLBI. As can be seen in Figure 2-6, approximately 1,400 hours of domestic and overseas observations are being made from 2015 to 2019. From 2018 onward, the ratio of domestic observations has been increased slightly.

Figure 2-5. The Korean Space Geodetic Observation Center and the Sejong VLBI Antenna

Figure 2-6. Annual observation hours for the Sejong VLBI (KVN: Korean VLBI Network)

The technical specifications of the Sejong antenna are presented in Table 2-1. The Sejong VLBI has a Cassegrain main reflector having a 22M diameter, and a total of four S, X, K, and Q band receivers. The S and X band receivers are mainly used for IVS observation, while the K and Q band receivers are used in observations for the KASI VLBI Network and the East-Asia VLBI Network (EAVN).

Table 2-1. Sejong Antenna Specifications

Parameters	Sejong VLBI
IVS letter codes	Sejong (KV)
CDP number	7368
DOMES number	23907S001
Location	127°.18′E 36°.31′N Elevation 177m
Diameter of main reflector	22m
Antenna type	Shaped Cassegrain
Aperture efficiency	about 60%
Pointing accuracy	0.0131°
Reflector surface accuracy	$100\mu m$
Operation range	AZ: ±270° EL: 0 ~ 90°
Slew speed	5°/sec (AZ and EL)
FS Version	9.10.4
Data acquisition Recorder	K5

**Table 2-2. Receiving system of the Sejong VLBI**

Band	S	X	K	Q
Freq.[GHz]	2.1~2.6	8.0-9.0	21-23	42-44
Receiver noise temp.	< 20K	< 30K	< 50K	< 80K
Polarization	R,L	R,L	R,L	R,L
SEFD	1,000	800	-	-
Aperture efficiency	0.6	0.6	0.6	0.6

Two different systems, which are Mark6 and K5, are used to record observation data from the Sejong VLBI. Recently, existing equipment is being upgraded, including the adoption of DBBC3 digital back end equipment. As a correlator, DiFX software is being used to perform correlation analysis for domestic VLBI observation data in-house. A server cluster, connected to 10 servers, has been implemented, capable of storing and performing correlation analysis on approximately 250TB of data. Domestic observation data is being analyzed approximately 10 times per year.

KVN Reference Points

The Korean VLBI Network (KVN) is the first VLBI facility in Korea, with three 21-m radio telescopes in Seoul (Yonsei), Ulsan, and Jeju (Tamna) island, operated by KASI. KVN has been participating in K band (22 GHz) geodetic VLBI observations together with VLBI Exploration of Radio Astrometry (VERA) of the National Astronomical Observatory in Japan (NAOJ) on behalf of the KVN and VERA Array (KaVA) geodesy program since 2011.

For Astrometry and Geodesy, it is important to determine an accurate reference position, often called the invariant point (IVP), of the radio telescope and to monitor the variation caused by crustal movement and gravitational deformation. To determine the IVP of KVN telescopes, we performed geodetic surveys at the KVN Ulsan and Tamna sites in a conventional way for the first time in 2017. Since the IVP is the intersection of the vertical (Az) and horizontal (El) axes, it is not directly accessible in most cases. Shown in Figure 2-7, the IVP marked in bold on the Az axis is the invariant point to be determined. IVP_1 and IVP_2 are the nearest points on the Az axis. $\overrightarrow{a_1}$ and $\overrightarrow{a_2}$ represent the nearest distance vectors from the El axis perpendicular to the Az axis.
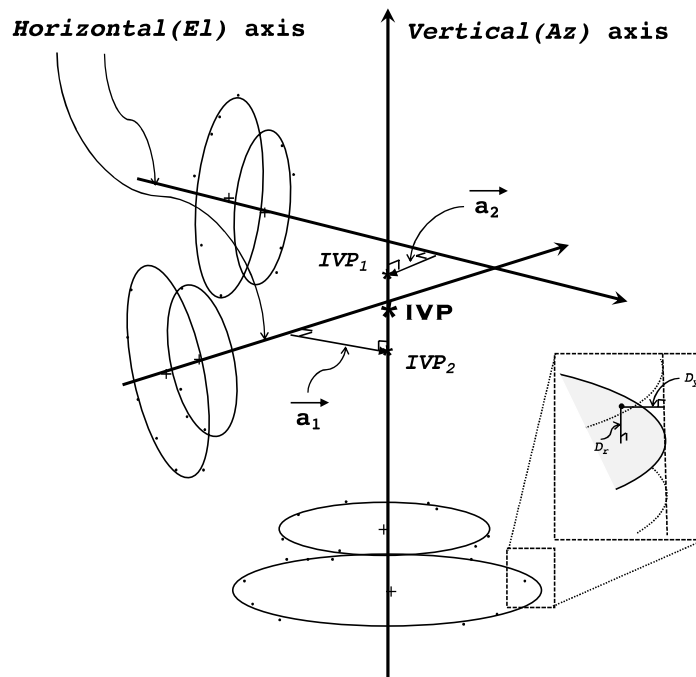
Figure 2-7. Illustration of IVP determination

Based on the results of the optical survey using Leica Nova MS60 Multistation, the targets form circles and arcs from the Az and El surveys, respectively. And the Az and El axes were estimated by applying 3D least-square line fitting method that minimizes the distance between the center points of circles calculated from the 3D circle fitting of target positions as shown in Figure 2-8 and 2-9.
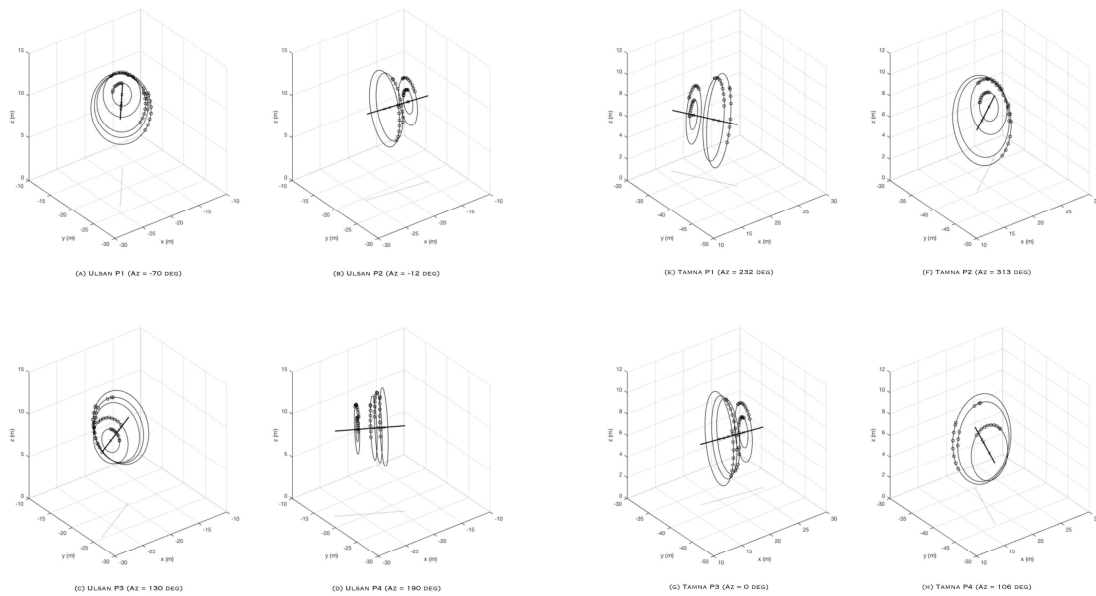
Figure 2-8. The results of 3D circle fitting for the El axis (Yoo *et al.*, 2018)
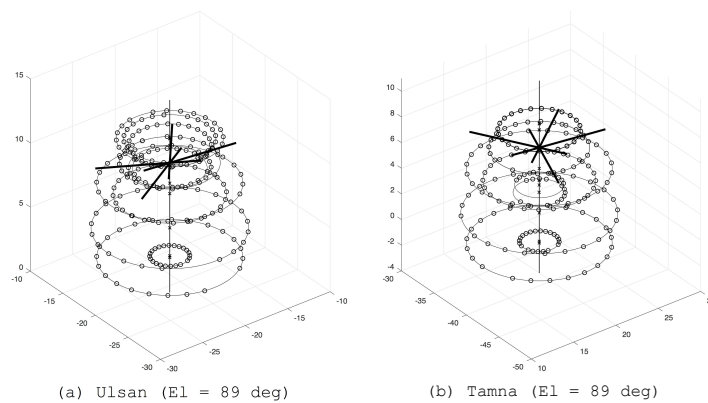
Figure 2-9. The results of 3D circle fitting for the Az axis (Yoo *et al.*, 2018)

In order to obtain the 3D geocentric coordinates of the IVP, the Helmert transformation were used to convert coordinates from the local frame in which the IVP survey can be performed to the geocentric frame. The geocentric coordinates of the IVP in ITRF2014 are listed in Table 2-3.

Table 2-3. KVN IVP Coordinates in ITRF2014

IVP	Ulsan 2017 Nov. 23, UT12:00	Tamna 2017 Dec. 06, UT12:00
X	-3287268.72004	-3171731.72457
Y	4023450.07902	4292678.45749
Z	3687379.93904	3481038.73301

Also, the axis-offsets caused by the telescope type, imperfections in construction, and gravitational deformations were estimated as 0.86 ± 0.49 mm for Ulsan and 2.43 ± 0.45 mm for Tamna. Based on the IVP determination of the KVN Ulsan and Tamna telescopes, high precision astrometric and geodetic VLBI observations using KaVA and EAVN will be promoted, especially at higher frequencies (22/43 GHz). In addition, these results will provide an important basis for the multi-frequency VLBI phase referencing, which is capable of constraining the amount of delay errors separately, so that a new prospect on astrometry and geodesy will be explored with the KVN. For the KVN Yonsei located in Seoul, we are planning to use the gimbal-mounted GNSS antennas as an alternative method due to the limited area near the site for optical survey.

2.3 SLR

Sejong ARGO-M

KASI has completed the ARGO (Accurate Ranging system for Geodetic Observation) project to develop one mobile and one fixed SLR systems, ARGO-M and ARGO-F respectively. The ARGO-M SLR system was developed and installed temporarily at the KASI headquarters in 2012, and system improvements were made in 2014. In July 2015, the system was relocated to Sejong and is under regular operation phase. Since January 11, 2016, Sejong SLR Station has been providing official data to ILRS. In particular, it is capable of making observations at a high repetition of 5 kHz, thus enabling greater precision in research.
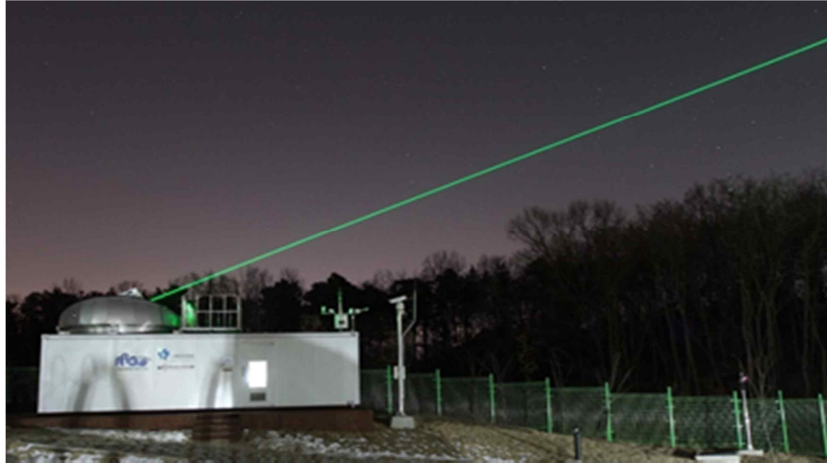
Figure 2-10. Sejong SLR Station (ARGO-M)

Figure 2-11. Registration of Sejong SLR Station in ILRS

Geochang ARGO-F

Having established its SLR system and adaptive optics system in November 2017, Geochang SLR Station is currently conducting test observations. While Sejong SLR Station can track medium Earth orbit satellites (approx. 24,000 km) with its 0.4 m primary mirror, it is unable to track satellites in geostationary orbit (36,000 km). Equipped with a 1.0 m primary mirror, Geochang SLR Station can track satellites in low Earth orbit (LEO), medium Earth orbit (MEO), and geostationary orbit.

Figure 2-12. Geochang SLR Station (ARGO-F)
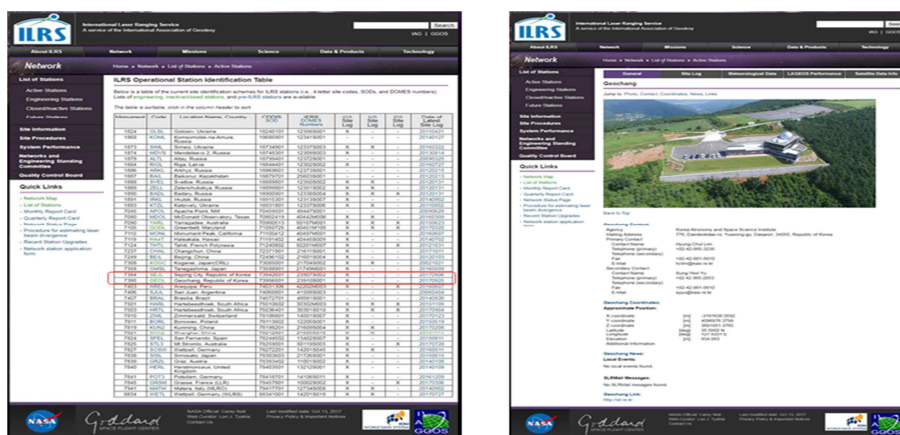
Figure 2-13. Registration of Geochang SLR Station in ILRS

2.4 GGOS

Local Tie at the Sejong GGOS Site

The GGOS site integrates space geodetic systems that previously operated independently of one another, and aims to provide a reference coordinate, necessary for geodetic observations, as well as high-precision data for the determination of Earth's rotation parameters. It is certified and managed by the GGOS committee of IAG.

Sejong SLR Station of KASI and the nearby VLBI and GNSS stations of the Space Geodetic Observation Center of NGII will contribute to determining the ITRF and EOPs. Since each station utilizes different space geodetic techniques, their relative positions must be precisely determined to ensure the accuracy of the resulting reference frame.

As shown in figure 2-14, each pillar around the Sejong SLR Station was designed to be solid from the deformation due to annual and daily temperature changes. In consideration of inter-visibility with Pillar 1 at the NGII Center, Pillars A, B, and C were given heights of 3,100 mm, 1,000 mm, and 1,700 mm, respectively.
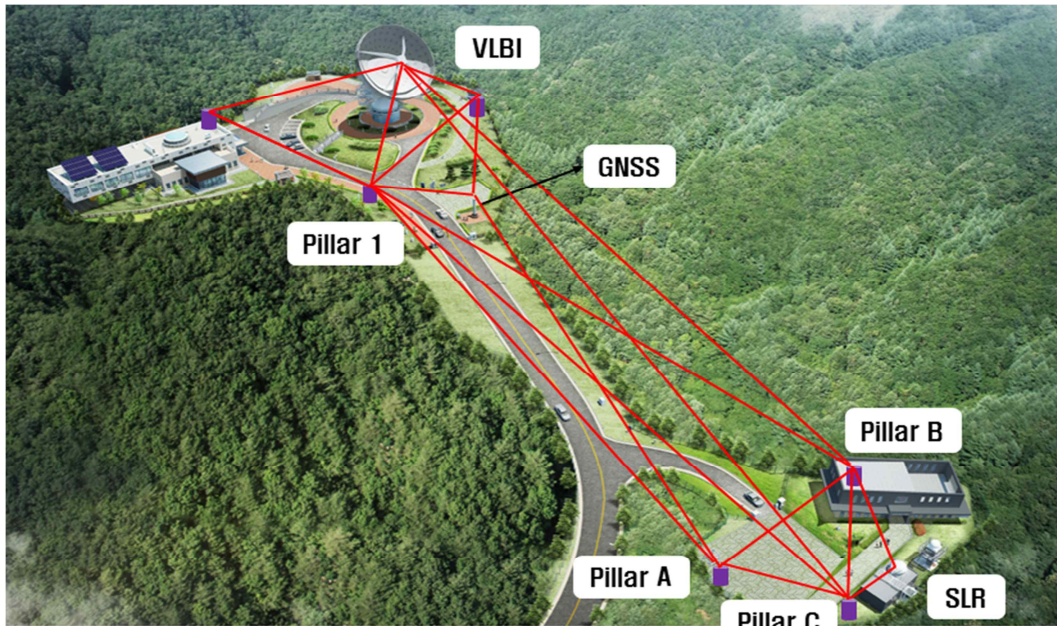
Figure 2-14. Local tie survey pillar installation at Sejong GGOS Site

From the second quarter of 2019, the local tie survey between VLBI-GNSS-SLR will be started. Measurements will be taken four times a year, and the results will be released in the form of a quarterly report.
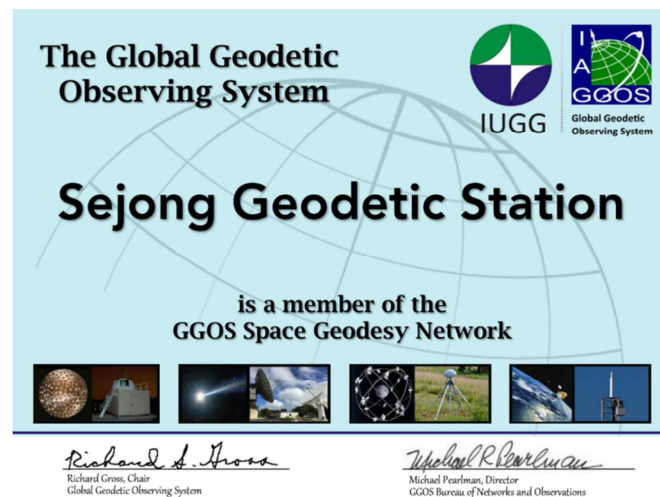
Figure 2-15. The certificate of Sejong GGOS Site (May 2019)

3. GRAVITY FIELD

National Control Point

The National Control Point (NCP) is a measured point providing basic position information for national base map and land development. The NCP in Korea, based on the Act on the establishment, management, etc. of spatial data, consisted of 7 types for land and 2 types for maritime affairs: VLBI, Satellite control point (GNSS CORS), Unified control point, Triangulation point, Benchmark, Gravity point, Magnetic Point; Hydrographic point and Territorial base point. Among above, NGII has determined the NCPs for land which is the hierarchy shown in Fig. 3-1.
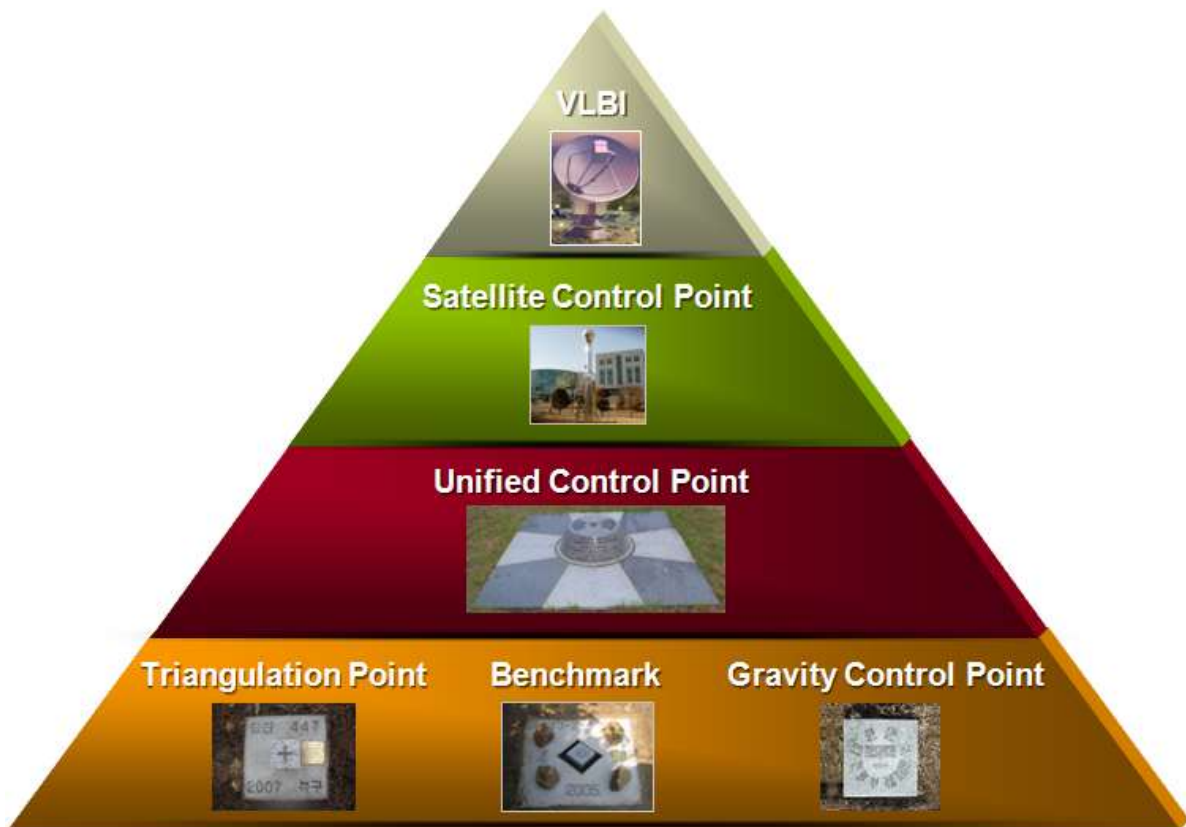
Figure 3-1. The hierarchy of national control points (NCP) in Korea

Unified Control Point

In the recent years, one of the dominant changes in Korean geodetic network is the activities

on the establishment of the Unified Control Points (UCP). The UCP provides the geodetic coordinates, ellipsoidal height, orthometric height and the gravity value at the same point. The objective is to fully utilize the satellite positioning technology and to establish the complete compatibility in worldwide coordinate system. On top of that, scientific and engineering data being provided at the same point with accurate spatial information is expected to enhance research quality so that more detailed analysis on physical phenomena could be performed. From 2008 until 2019, there are a total of 5,500 markers installed all over the country with 3 km ~ 5 km spacing.

Gravity Survey

NGII also maintains the gravity control point which consists of absolute and relative gravity points. Currently, 20 absolute gravity points have been established by the measurement of FG5 absolute gravimeter and regularly measured in 5-year intervals. In order to achieve denser gravity data over the country, relative gravity surveying has been conducted by CG5 at a part of the NCPs, and around 15,000 points have been measured until 2019.

Korea National Geoid Model

NGII has developed Korea National Geoid (KNGeoid) model since 2009 in order to provide the optimal precise geoid over whole Korean peninsula. After developed the KNGeoid14, the KNGeoid18 (NGII, 2018) was newly developed with a higher precision and a wider range, by using measured data until 2017. The comparison of the version of the KNGeoid is shown in Table 3-1.

In next years, additional measurements will be obtained on outlying areas of the country to construct a more precise geoid model. In addition, to support the adoption of orthometric height taking advantage of GNSS measurements in practical fields, related regulations are under consideration.

Table 3-1. Comparison of KNGeoid14 and KNGeoid18

Item	KNGeoid14	KNGeoid18
Precision		
Gravimetric model	6.81cm	4.38cm
Hybrid model	3.55cm	2.33cm
Coverage		
Latitude	33˚ ~ 39˚	33˚ ~ 39˚
Longitude	125˚ ~ 131˚	124˚ ~ 132˚
Resolution	0.01636˚	0.01636˚
Used data		
Global gravity model	EGM08	XGM2016
Gravity data (land)	9,455 points	12,117 points
GNSS/Leveling data	1,034 points	2,791 points

4. EARTH ROTATION AND GEODYNAMICS

4.1 Earth Rotation

A Machine Learning Algorithm and Topological Data Analysis

Precise analysis of Earth rotation metrics is crucial in understanding changes to the Earth environment and for short- and long-term climate change forecasting. Development of VLBI has made possible extremely precise observation of Earth's polar motion. NGII and Ajou University have proposed an accurate and efficient method for detecting motion anomalies in VLBI data through topological data analysis and deep learning (NGII, 2018).

Theoretical models for Earth rotation metrics are assessed using convection, glacial movement, crust movements, ocean base pressure, atmospheric pressure and wind direction as parameters. Actual observation values and theoretical model values can be visualized as shown in Figures 4-1 and 4-2.
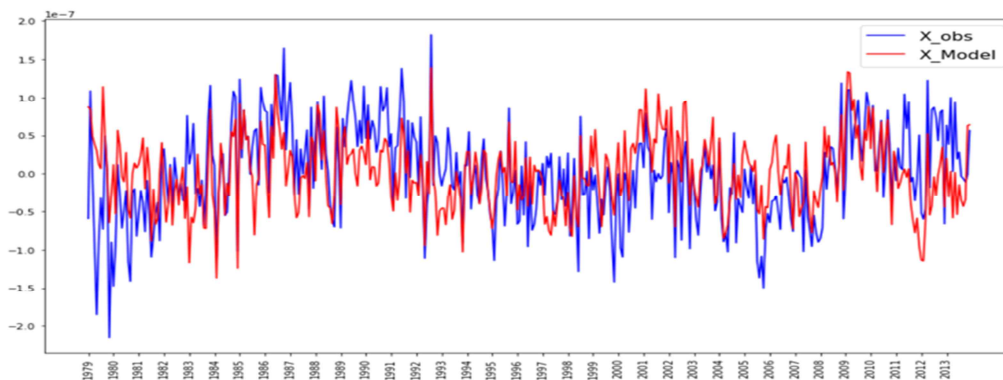
Figure 4-1. Observed and theoretical values for time-series data on Earth rotation metrics (X component)
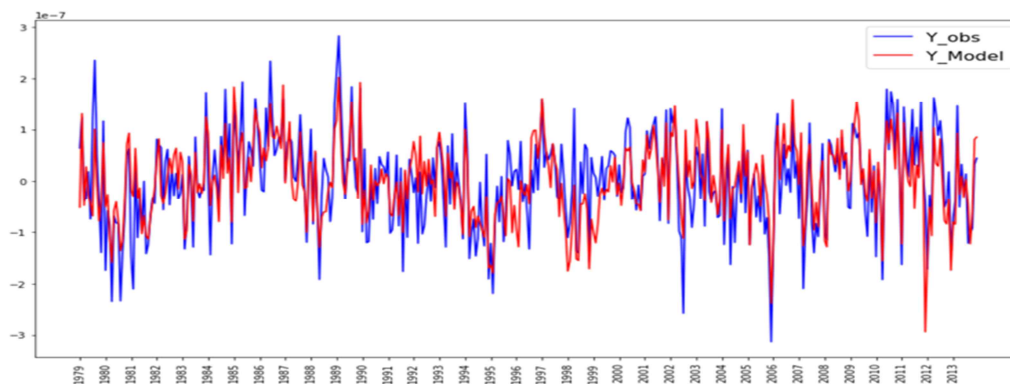
Figure 4-2. Observed and theoretical values for time-series data on Earth rotation metrics (Y component)

Earth rotation observation data is a collection of values which are determined by numerous parameters including solar and lunar gravity, and movement of the Earth's atmosphere and crust. In this data exists multi-dimensional topological space created by these parameters. Accordingly, Earth rotation data obtained through simulation experiments based on theory is expressed as the multiplication product of the probability distributions for the respective parameters, expanding data size. The data obtained through VLBI observations also has high spatial and temporal resolution, and is data of a massive scale. Finding regular signal patterns apparent in this big data to understand Earth rotation, and detecting signal anomalies divergent from theoretical values or regular observation patterns involves mathematical and computational difficulty. In particular, comparing theoretical values found using known parameters and actual observation data to find parameter probability distributions or discover anomalous patterns requires consideration of both noise in observed values and theoretical model uncertainties. Accordingly, development of high-precision analytical methods is necessary.

The National Geographic Information Institute and Ajou University, in keeping with such requirements, wish to propose two big data analysis techniques for analysis of big data on Earth angular momentum deduced from VLBI observation data. The first is a topological data analysis method wherein observation signals are mathematically interpreted by calculating the topological shape of data in the topological space where the observation data exists, and performing deep learning based on such interpretation to analyze data. The second method involves use of deep learning using data obtained through theoretical models and observational big data, finding patterns in changes to Earth angular momentum and analyzing signal anomalies.

For analysis of residuals between observed and theoretical values for Earth rotation metrics, a method of Earth rotation metrics data analysis using topological data analysis and convolutional neural networks was devised. This is because the conventional methods of signal analysis, including Fourier analysis, spectrum analysis and wavelet analysis are limited to linear models and are unsuitable for signal anomaly detection. Topological data analysis is carried out by mapping given time-series data to a specific topological space, and calculating homology groups for each dimension of the topological space. The observed and model values for Earth rotation data given for topological data analysis were projected onto a two-dimensional sphere, and the homology groups for the topological space were calculated.

At the respective points on the topological space formed by projection onto a two-dimensional sphere, the reference distance t is increased. If the distance between two points is less than t, the two points are connected. As t gradually increases, first-dimension and second-dimension groups are created and disappear, and this data is used to output a persistent diagram. The resulting persistent diagrams show that the observed and model values for Earth rotation metrics data form different topological spaces.
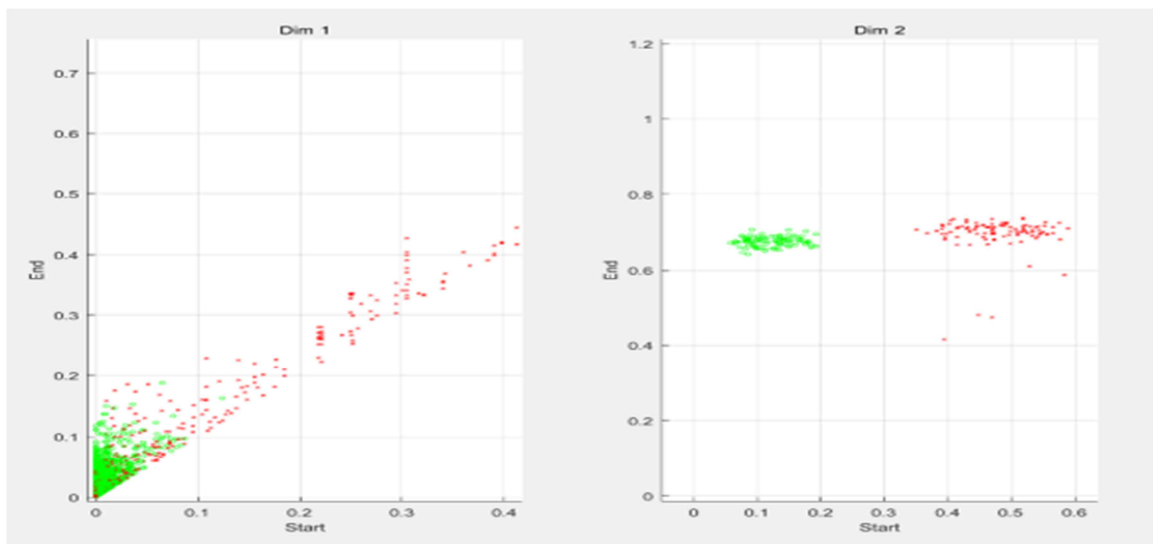
Figure 4-3. Persistent diagram for topological space with Earth rotation metrics data projected onto two-dimensional sphere (Green dots: observed values; Red dots: theoretical values)

Upon visual inspection of the graphs for observed and theoretical Earth rotation metrics data, it is difficult to identify whether or not the theoretical model explains natural phenomena well, or whether anomalies which the model cannot explain exist. The convolutional neural network model and other deep learning models have recently exhibited high performance in classification models and regression models. Two-dimensional convolutional neural networks, which are exhibiting particularly high performance in the field of computer vision, use small rectangular filters to discover patterns in regional data within an image. By the same principle, applying a one-dimensional convolutional neural network to time series data, it is possible to find patterns which occur repetitively in data. In the present study, learning was performed with observed values and theoretical model values with added random Gaussian noise and a convolutional neutral model classifier. By carrying out tests with random given data, classifier performance was quantified. 10,000 data were generated for each of observed values and theoretical model values for learning, adding random Gaussian noise.
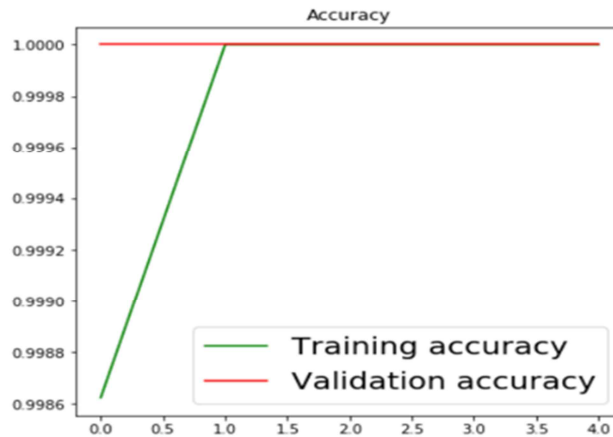
Figure 4-4. Results of classifier accuracy assessment using test data

Figure 4-4 illustrates classifier performance when a one-dimensional neural network was taught using data for the entire period (January 1979 to December 2013, 420 months). From the fact that the given observed values and theoretical model values were accurately classified using a simple two-layer depth one-dimensional convolutional neural network, it was confirmed that there were periods where the theoretical model was unable to explain actual metrics.

To detect the existence of Earth rotation signals in periods of scales smaller than above, data was sequentially horizontally shifted in 12-month units to form a data set. The one-dimensional convolutional neural network classifier model was taught using the data set, and the results of classifier performance quantification are shown in Figure 4-5. This Figure illustrates the ratio of incorrect results from the one-dimensional SNN classifier when using x-axis component data for Earth rotation metrics. Values closer to 0 indicate higher classifier accuracy, and the results imply that the theoretical model does not sufficiently explain natural phenomena. Conversely, values closer to 0.5 indicate the classifier was unable to distinguish between observed and theoretical model values.

Through topological data analysis, a clear difference was confirmed between the topological spaces formed by observed and theoretical model values for Earth rotation metrics. From the fact that a shallow, 2-layer depth convolutional neural network classifier was able to accurately distinguish observed values and model values with added noise, it could be known that the Earth rotation metrics theoretical model was unable to sufficiently explain actual natural phenomena. In future research, a means of predicting actual phenomena and detecting movement anomalies through a theoretical model for Earth rotation metrics based on parameters such as atmospheric movement, crust movement, and glacial movement, etc.

while using a recurrent neural network taught using past data will be proposed.
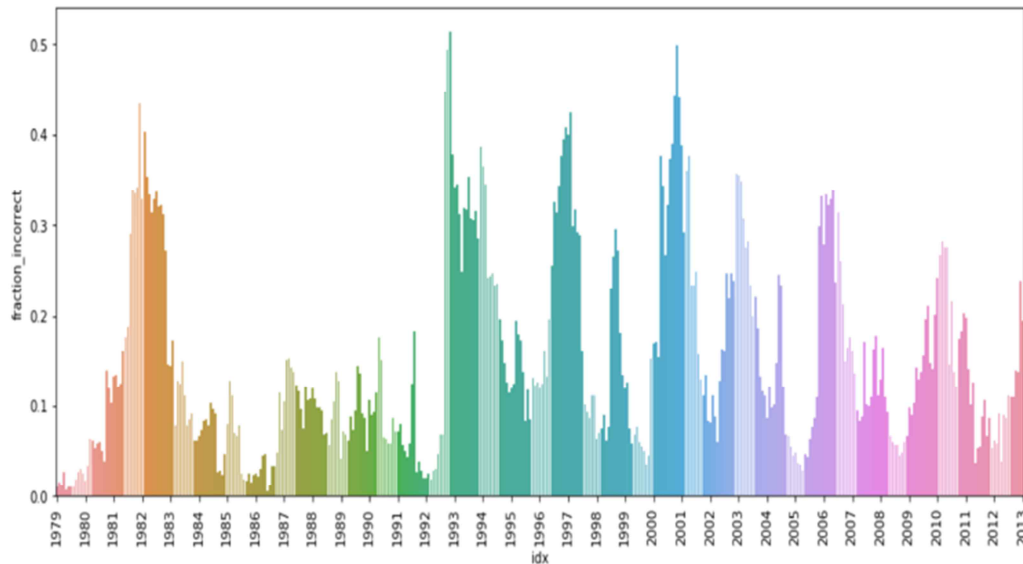
Figure 4-5. Ratio of incorrect results from one-dimensional CNN classifier

Atmospheric Excitation

The atmosphere strongly affects the Earth's spin rotation in wide range of timescale from daily to annual. Its dominant role in the seasonal perturbations of both the pole position and spinning rate of the Earth is once again confirmed by a comparison of two recent data sets; i) the Earth orientation parameter and ii) the global atmospheric state.

A daily basis Earth's spin rotational time series data by the name of EOP 08 C04 (Bizouard & Gambis 2009) was obtained from the IERS website for this study (http://www. iers.org/IERS/EN/IERSHome/). The EOP C04 dataset is composed of the pole position (x_p, y_p) and the spin change in terms of excessive amount of length of day ($\Delta l.o.d.$). ECMWF datasets for global atmospheric pressure and wind velocity for the time span between Jan 1981 and Dec 2015 were extracted and processed to derive the atmospheric excitation function (http://www.ecmwf.int). Two contributions from: i) excessive mass (pressure) and ii) motion (wind) were evaluated separately, and then summed together resulting the total atmospheric excitation functions (χ_1, χ_2, χ_3) to be compared with the observed excitation inferred from polar motion data.

From the polar motion and *l.o.d.* time series of EOP C04, the observed excitation functions were computed. And the atmospheric excitation functions acquired from ECMWF data. To

better compare the two kinds of excitation functions, those parts of five year time span (2010-2015) are shown again on three separate figures (Fig. 4-6 (a)-(c)). In all these three comparisons (a-c), similarities between the observed excitation and the calculated atmospheric excitation are noticeable. From the excitation function $\chi_3 obs$ shown in Fig. 4-6 (c), it is found that *l.o.d.* is shorter by about -0.65 millisec in late June - early September and longer by +0.65 millisec from winter to spring time. Seasonal variations are not quite clear in the two (observed and atmospheric) excitation time series of χ_1, while one-year periodicity is distinct in both sets of χ_2 and χ_3. The amplitude of atmospheric excitation χ_2^{atm} slightly exceeds that of observed one. Correlation of observed and atmospheric excitation is best for χ_3; however, high frequency terms are much reduced in the atmospheric excitation χ_3^{atm}.
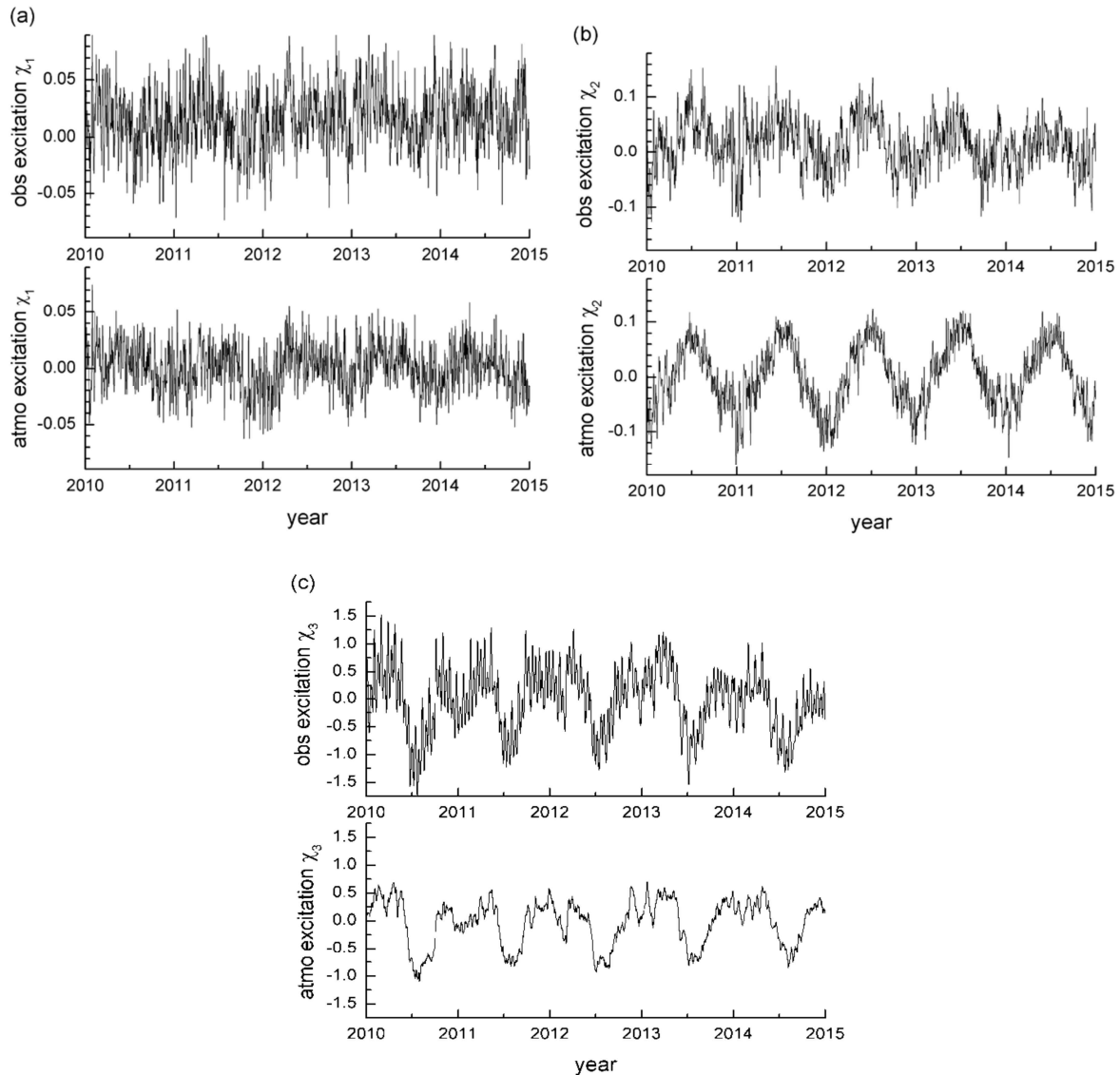
Figure 4-6. Three sets of both observed and calculated excitation functions χ_1, χ_2, χ_3 redrawn for a five-year time span between Jan 1, 2010 to Dec 31, 2014. Units are [arcsec] for χ_1, χ_2 and [10^{-8}] for χ_3 (Na *et al.*, 2016)

Deceleration & Acceleration (New Calculation)

The global oceanic/atmospheric tides exert decelerating/accelerating secular torques on the Earth rotation. We developed new formulations to accurately calculate amounts of two kinds of secular tidal torques. After Melchior, we found that an additional factor 1+k-l = 1.216, which has been formerly neglected, must be multiplied unto the tidal torque integral. By using our refined formulations and the recent oceanic/atmospheric global tide models, we found that: (i) semidiurnal oceanic lunar/solar tides exert decelerating torques of about -4.462 x 10^{16} / -0.676 x 10^{16} Nm respectively and (ii) atmospheric S2 tide exerts accelerating torque of 1.55 x 10^{15} Nm. Former estimates of the atmospheric S2 tidal torque were twice as large as our estimate due to improper consideration of loading effect. We took the load Love number for atmospheric loading effect from Guo et al. (2004). For atmospheric loading of spherical harmonic degree two, the value of k'= -0.6031 is different from that for ocean loading as k' = -0.3052, while the latter is currently used for both cases e ocean/atmospheric loading e without distinction. We discuss (i) the amount of solid Earth tidal dissipation (which has been left most uncertain) and (ii) secular changes of the dynamical state of the Earth-Moon-Sun system. Our estimate of the solid Earth tidal torque is -4.94 x 10^{15} Nm.

Tidal force on the Earth is schematically illustrated in Fig. 4-7 a. Ocean tide is one of the largest periodic perturbations of the Earth, and its prediction has been important both in the scientific communities and civic societies. Due to tidal dissipation, there exists certain amount of phase delay in ocean tides. As a result a decelerating torque is being exerted to the Earth (see Fig. 4-7 b). Although pioneers suspected this interaction should occur in the Earth-Moon system, they could not figure out its amount until the global ocean tide modeling being feasible. Compared with the first stage ocean tide models in 70s and 80s, the model accuracy and resolution are being enhanced by one order of magnitude nowadays. It has been our first objective in this study to make more accurate estimate of the secular ocean tidal torque. There were two former investigations on the same issue but with more or less different approaches two or one decade ago (Ray *et al.*, 1999, Mathews & Lambert, 2009). Both of them neglected the factor -1+k-l = 1.216.
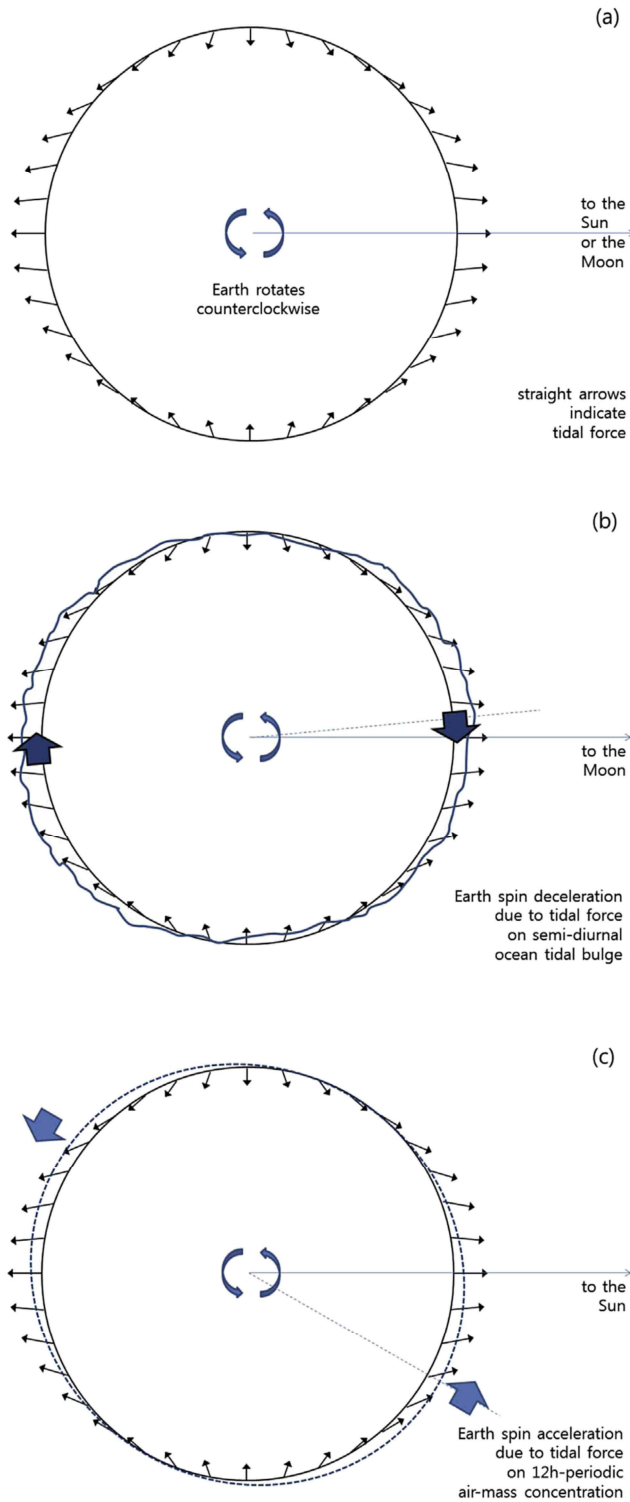
Figure 4-7. Schematic figures of tidal force exerting on the Earth and comparison of accelerating torque by oceanic M2 tide and decelerating torque by atmospheric S2 tide: (a) Tidal force vector on the surface of the Earth, (b) Description of oceanic M2 tidal torque and associated equivalent phase delay, (c) Description of atmospheric S2 tidal torque and associated phase lead. (Na *et al.* 2019)

Due to periodic solar insolation unto the Earth, two harmonic oscillations of periods of 12 and 24 h exist in the barometric pressure over the globe, which are referred as S2 and S1 atmospheric tides respectively, although they are not caused by lunisolar tidal force. Unlike ocean tide, the 12 h period barometric pressure records maximum about 2 h early in most places and therefore exert accelerating torque (see Fig. 4-7 c). Munk and MacDonald early estimated the atmospheric tidal acceleration on Earth rotation (Munk & McDonald, 1960). Later others occasionally made estimates of atmospheric tidal acceleration (Lambeck, 1980, Ray *et al.*, 1999). However their results overestimated it due mainly to inaccurate treatment of loading effect. Atmospheric tide models are also being updated as well from its early versions (Ray & Ponte, 2003, Schindelegger, 2014).

As our new calculation, the secular tidal torques exerted to the Earth by ocean tide and atmospheric tide are found as -5.14×10^{16} and 1.55×10^{15} Nm respectively. The sum of these two tidal torques is -4.99×10^{16} Nm. Ocean tidal torque -5.14×10^{16} Nm is composed of torques of two distinct origins - the Moon and Sun.

Lunar tidal torque -4.46 x 10^{16} Nm decelerating the Earth should be accompanied with opposite torque exerting to the Moon. Due to obliquity angle of about 23.5°, secular torque on the Moon is effectively reduced by a factor of 0.917. Corresponding increase rate of lunar distance is 1.09 x 10^{-9} m/s. Present lunar recession rate of 3.8 cm/yr or 1.22 x 10^{-9} m/s is larger than this amount; 1.09 x 10^{-9} m/s, and the difference could mainly come from tidal dissipation in the Earth's mantle and crust. Although the Earth's body tide itself can be predicted quite accurately, inelasticity and energy dissipation inside the Earth is not well known. Based on our estimates above, we conclude that body tidal torque is -4.94 x 10^{15} Nm, which is about 10 percent of ocean tidal torque.

4.2 Geodynamics

Atmospheric loading on the Korean Peninsula

Displacement of the Earth's surface due to atmospheric loading has been recognized since a century years ago, and its accurate estimation is required in present day geodesy and surveying, particularly in space geodesy. Atmospheric load deformation in continental region can readily be calculated with the given atmospheric pressure field and the load Green's function, and, in near coastal area, approximate model is used for the calculation. The changes in the Earth's atmospheric circulation and the seasonal variation of atmospheric pressure on two hemispheres of the Earth are the each main causes of variation of the Earth's spin angular velocity and polar motion respectively. Wind and atmospheric pressure do the major role in other periodic and non-periodic perturbations of the positions in the Earth's reference frame and variations in the Earth's spin rotational state. In this reviewing study, the developments of related theories and models are summarized along with brief description of phenomena, and the geodetic perturbing effects of a hypothetical typhoon passing Korea are shown as an example.

We calculated the deformation of the Korean peninsula induced by a hypothetical typhoon passing through it. The assumed path is drawn with five particular locations on its way (Fig. 4-8 a). The central pressure and radius of the typhoon were taken constant as 950 hPa and 150 km respectively at all the five locations. The simulated deformation due to the low

atmospheric pressure of the hypothetical typhoon placed at the each location was acquired repeatedly and illustrated (Fig. 4-8 b-f). Maximum uplift in the peninsula slightly exceeds 6 mm, when the main parts of the typhoon lie on the peninsula.

We used the load Green's function calculated for the IASPEI Earth model (Na and Baek, 2011), because the physical properties of the Earth's crust and upper mantle around Korea is closer to that one. Unlike the Yellow Sea and the South China Sea (called 'South Sea' in Korea), the Korea-Japan Sea (called 'East Sea' in Korea) has narrow channels to outer open oceans, therefore, the 'inverted barometer' concept need to be used differently with treating the Korea-Japan Sea as a large lake. According to van Dam et al. (2010), a few millimeter errors were found during the atmospheric loading calculation in area of highly variable topography. Further investigations are needed on such points.

Seasonal Atmospheric Loading on Continents

Northern Eurasian continent has been regarded to contribute as the major source area, of which seasonal atmospheric pressure loading and unloading cycle leads to the annual wobble of the Earth. In the early days when reliable data of global coverage were not accessible, this dominance has remained as only a hypothesis. Nowadays, however, European Centre for Medium-Range Weather Forecasts and National Centers for Environmental Prediction produce reliable datasets, therefore, such unique feature has become clearer with quantitative evidences. Having both the Earth's polar motion and the global atmospheric state known with unprecedented accuracy, we hereby identify and scrutinize whether Siberia and Manchuria dominate the annual polar motion of the Earth.

Annual wobble is one of the two main components of Earth's wobbling motion. While Chandler wobble excitation mechanism has been controversial for a long time, it is evident that annual wobble is driven by geophysical phenomena having periodic seasonal variations. And it has been presumed since early times that Siberia does a noticeable role in the annual wobble excitation, i.e., periodic loading/unloading of air mass over the wide Siberian land may result in major contribution on the Earth's annual wobble.

Information of worldwide weather are gathered and assimilated in European Centre for Medium-Range Weather Forecasts (ECMWF) and National Centers for Environmental Prediction (NCEP) for the purpose of weather forecasting as well as to provide datasets necessary for scientific investigations. The 6-hr period global data coverage by ECMWF on
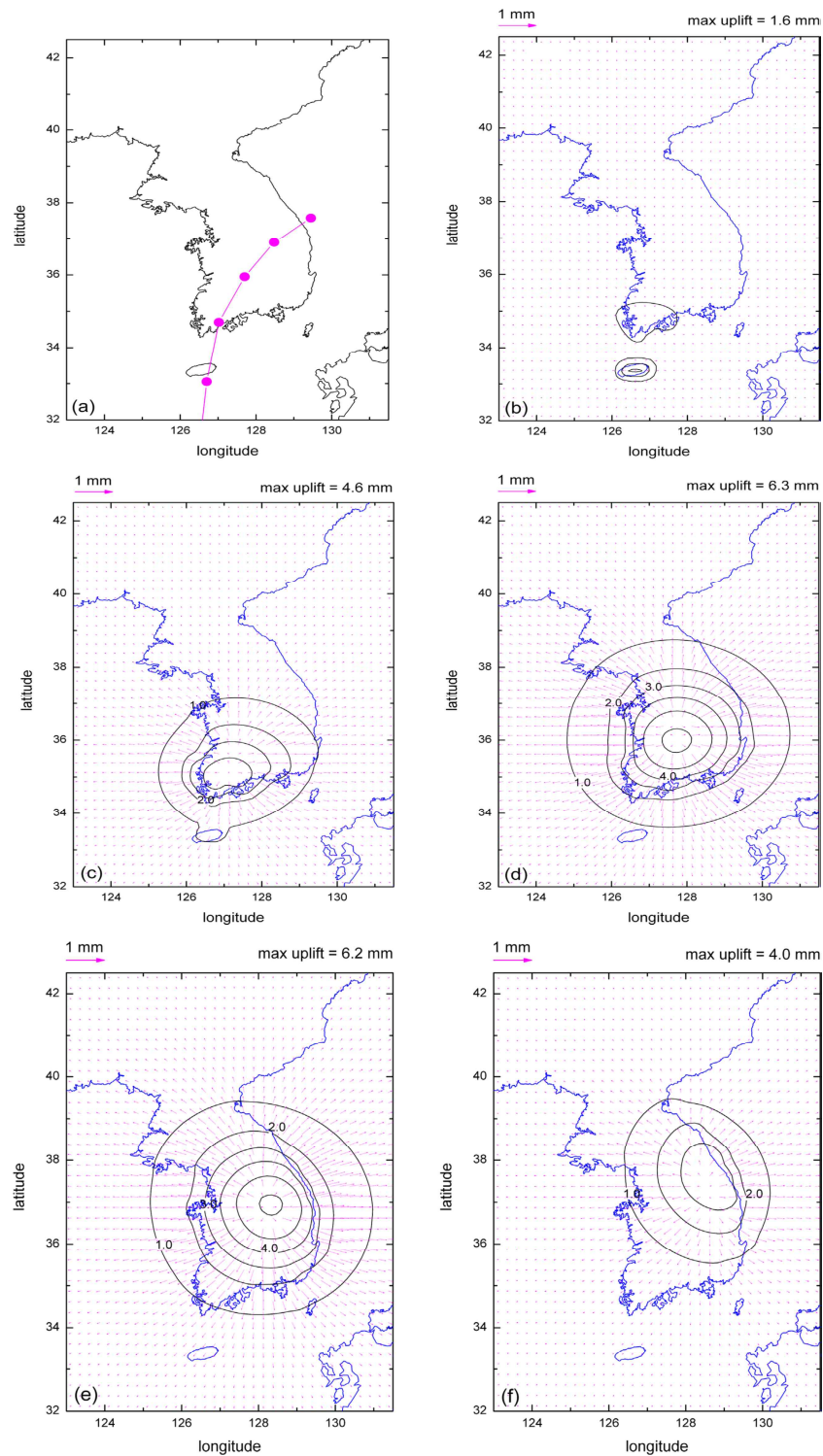
Figure 4-8. Demonstration of the atmospheric loading induced deformation due to a hypothetical typhoon: (a) Path of the hypothetical typhoon passing Korea, (b-f) Calculated vertical and horizontal displacement induced by the hypothetical typhoon placed at 5 each locations marked in (a). The contour lines correspond to equal uplift (contour interval: 0.5 mm in (b) and 1 mm in (c-f)), and the pink arrows represent horizontal displacements at grid points. (Na & Cho, 2015)

wind velocity and barometric pressure can be used to infer the atmospheric excitation of Earth rotation. We analyze monthly average values of differential surface atmospheric pressure from local yearly average in the year of 2016. On the northern part of Eurasian continent, i.e., Siberia and Manchuria, high atmospheric pressure exists from October to March, while low atmospheric pressure prevails from May to August. Although this seasonal loading/unloading cycle has been thought as the main input to annual wobble since the beginning of last century, reliable estimations have been deferred until the advent of accurate source of information, such as ECMWF dataset or comparable sort.

In this study, we compare (1) the observed geodetic excitation inferred from the recent polar motion data and (2) the calculated atmospheric excitation due to seasonal atmospheric loading/unloading on Northern Eurasia as well as four other continents, namely, North America, South America, Australia, and Africa. We used IERS EOP C04 and ECMWF atmospheric pressure datasets each. As the results, we have five-year (2010-2015) geodetic excitation function for χ_1 and χ_2. Each function consists of five components which are geodetic excitation, atmospheric excitation (wind and pressure), atmospheric excitation (wind only), atmospheric excitation (pressure only), and atmospheric excitation (pressure of Siberia and Manchuria).

We repeated the computation for atmospheric pressure excitation on other continents, North America, South America, Australia, and Africa. The amplitudes of the geodetic excitation and calculated excitation due to atmospheric pressure on the five continents are illustrated together in Fig. 4-9 for their comparison. It has been found that the atmospheric pressure loading/unloading annual cycle on Siberia and Manchuria gave rise to 15.61 milliarcsec excitation in χ_2 component, which is 54% of total excitation observed, while the same area gave rise to much smaller χ_1 excitation. The atmospheric loading/unloading on Australia gave rise to rather large excitation both on χ_1 and χ_2.
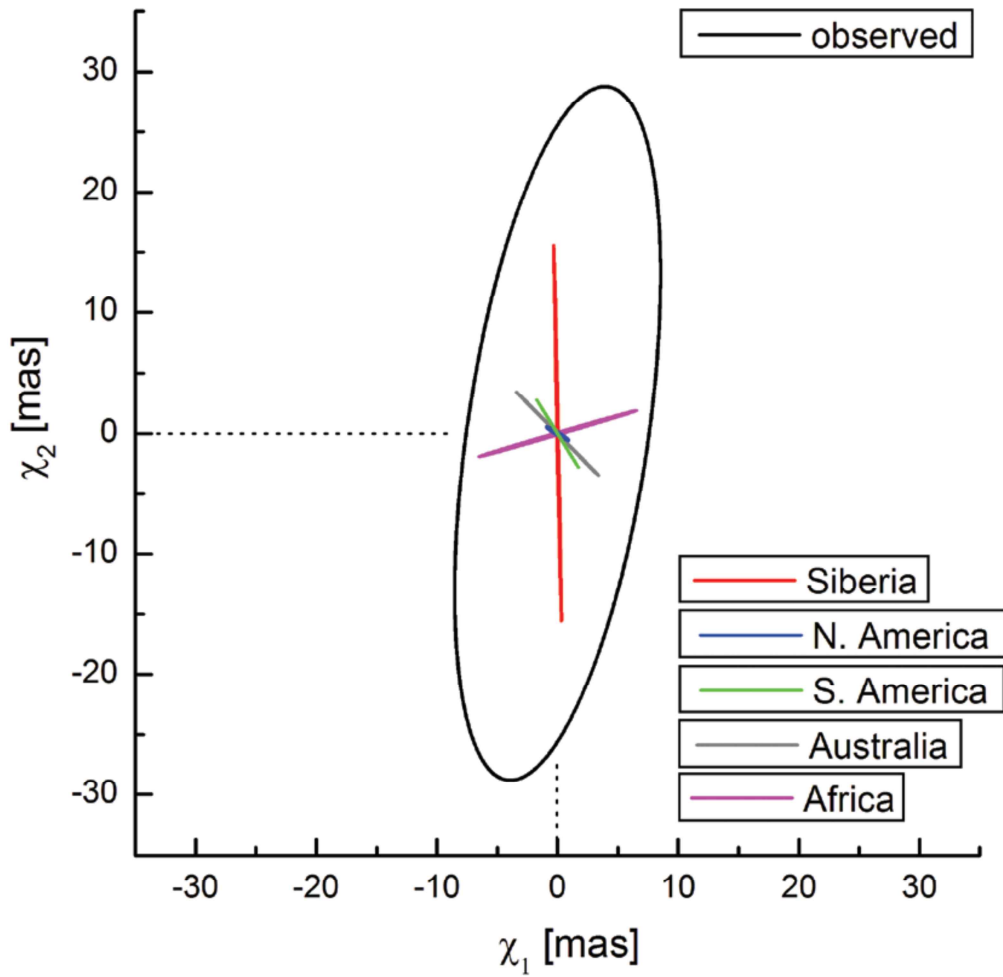
Figure 4-9. Comparison of geodetic excitation and five annual excitation fits on the atmospheric pressure loading/unloading on the 5 continents – Eurasia, N. America, S. America, Australia, and Africa. (Na *et al.*, 2018)

5. APPLICATIONS

5.1 GNSS Data Sharing Platform

The NGII uses PIVOT from Trimble and GNSmart from Geo++ to provide free VRS and FKP calibration signal services to the private sector. One million users use the Networked Transport of RTCM via Internet Protocol (NTRIP) based real-time calibration data service through each year, with usage increasing every year.
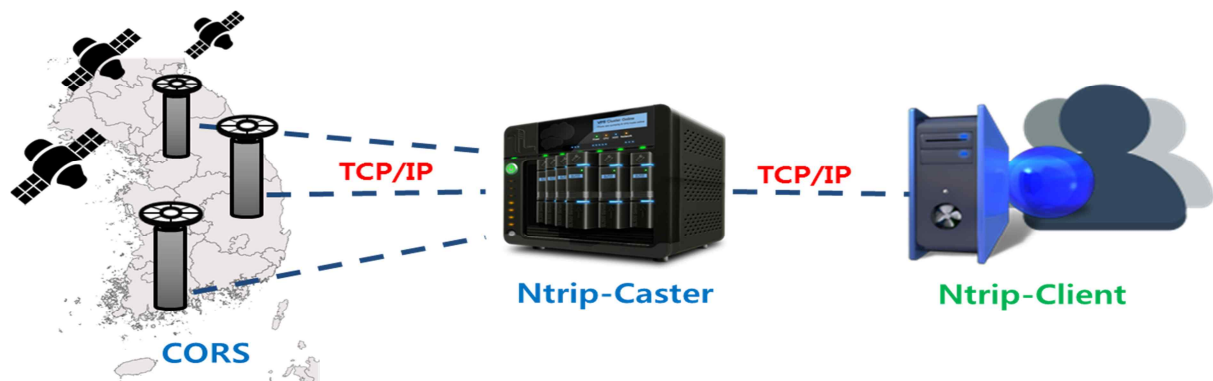
Figure 5-1. Ntrip calibration data service

Recently, addition of various communication protocols such as DMB and LTE is being considered to furnish additional services. Since 2017, through agreements with domestic broadcasters, Single-RTK calibration signals are being serviced using terrestrial DMB.

An State Space Representation (SSR) correction data service is also being prepared. Feasibility studies for adoption of new calibration signals, including positioning accuracy checks and other utilization of SSR correction signals, are being carried out, and depending on the results, private sector SSR correction data service will begin in 2020 at the earliest.

The NGII works with eight institutions to operate the GNSS Data Sharing Center in order to provide unified service using data from the GNSS CORS operated by domestic research institutes and universities. The GNSS Data Sharing Center gathers data from upward of 180 CORS operated by the respective institutions. This data is serviced through the website, and daily RINEX and RTCM are provided. RTCM is provided through the Ntrip server, and the respective CORS function as mount points to provide calibration signals.
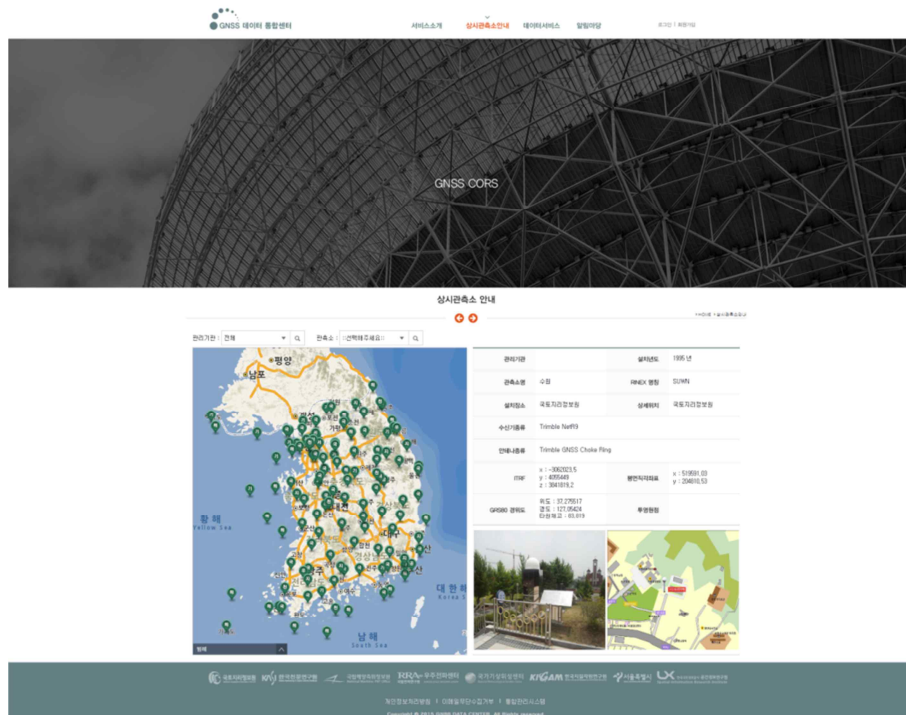
Figure 5-2. The webpage of the GNSS Data Sharing Center

5.2 Natural Hazards

Troposphere

Atmospheric water vapor is one of crucial gases for energy transfer and greenhouse effects. Nowadays GNSS meteorology enables continuous monitoring of the atmospheric water vapor in near real time. KASI developed GNSS precipitable water vapor (PWV) system in order to apply the PWV to numeric weather predictions in near real-time.

Figure 5-3 shows the near real-time GNSS PWV system that consists of Data PRocessing server (DPR), Data Receive and Service server (DRS), and Test and EValuation server (TEV). The DPR processes GNSS data and then retrieves PWV from estimated zenith total delay (ZTD) with an optimal mean temperature equation (MTE) for the Korean Peninsula. The DRS collects data from more than eighty permanent GNSS stations using NTRIP and provides the GNSS PWV to a user. The TEV is in charge of redundancy of the DPR. The GNSS PWV system uses three high performance computers to process enormous data in near real-time. In addition, Bernese GNSS software 5.2 produces a local network solution every

10 minutes using GNSS observation data that shifts every 10 minutes with a sliding time window of 24 hours.
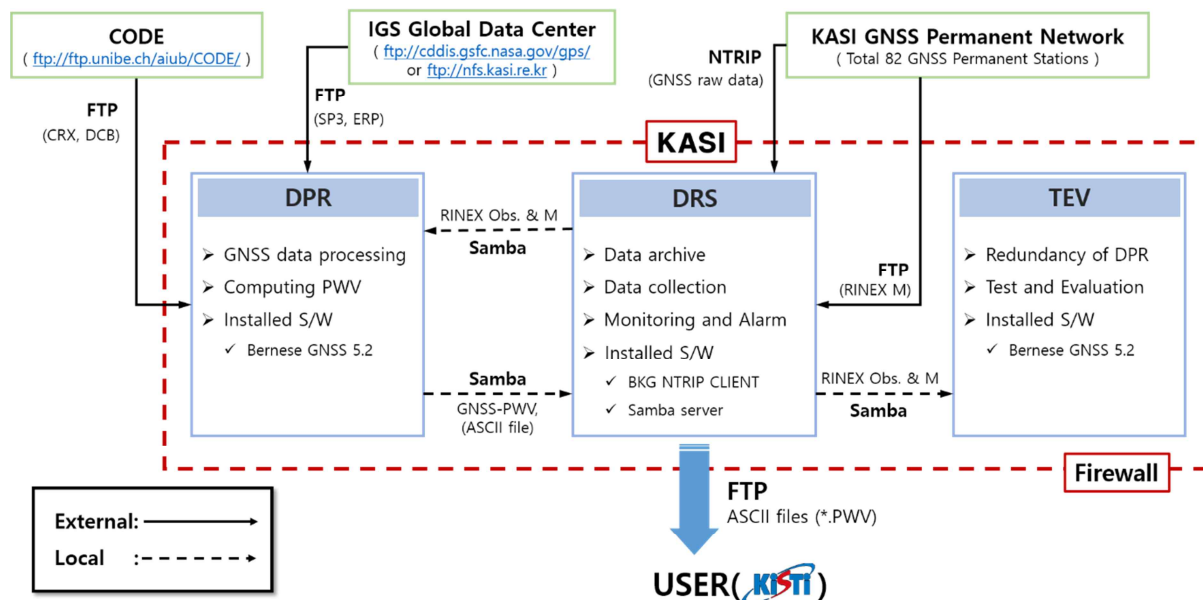
Figure 5-3. Near real-time GNSS PWV system

Several local mean temperature equation models (MTEs) had been developed and were compared with each other including a regional (Bevis et al., 1992) and a global (Mendes, 1999). Detailed information of the models are summarized in Table 5-1 (Wu, 2003; Ha & Park, 2008; Song &G.-Brzezinska, 2009; Song, 2009). Unlike the other annual models, Song I and Song II are seasonal corresponding to summer and winter respectively. As shown in Figure 5-4, each MTE shows different inclination. Thus, each MTE is separated big particularly in summer and winter range of the surface temperature.

Table 5-1. Summary of details of the mean temperature equations

Models	a	b	RS Sites	Periods
Bevis	0.72	70.2	U.S.	1989 – 1991
Mendes	0.789	50.4	Global	1992
Wu	0.968	1.056	South Korea	1998 – 2004
Ha	0.884	23.4	South Korea	1998 – 2005
Song I	1.01 (summer)	-12.35 (summer)	South Korea	2003 – 2005
Song II	0.97 (winter)	8.67 (winter)	South Korea	2003 – 2005
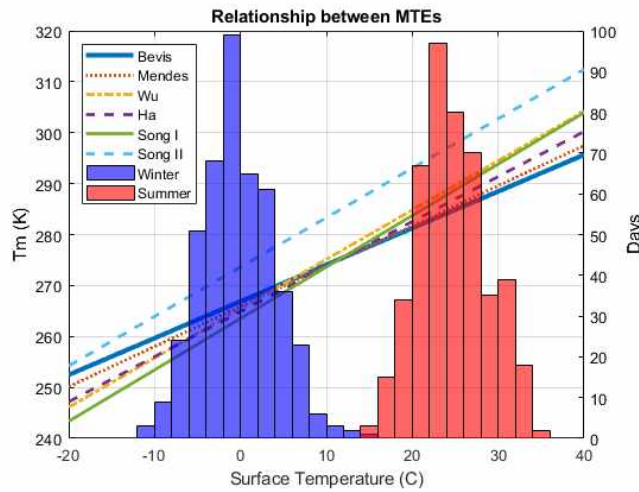
Figure 5-4. Comparisons between the MTEs with respect to surface temperature and histogram of surface temperature in summer and winter.
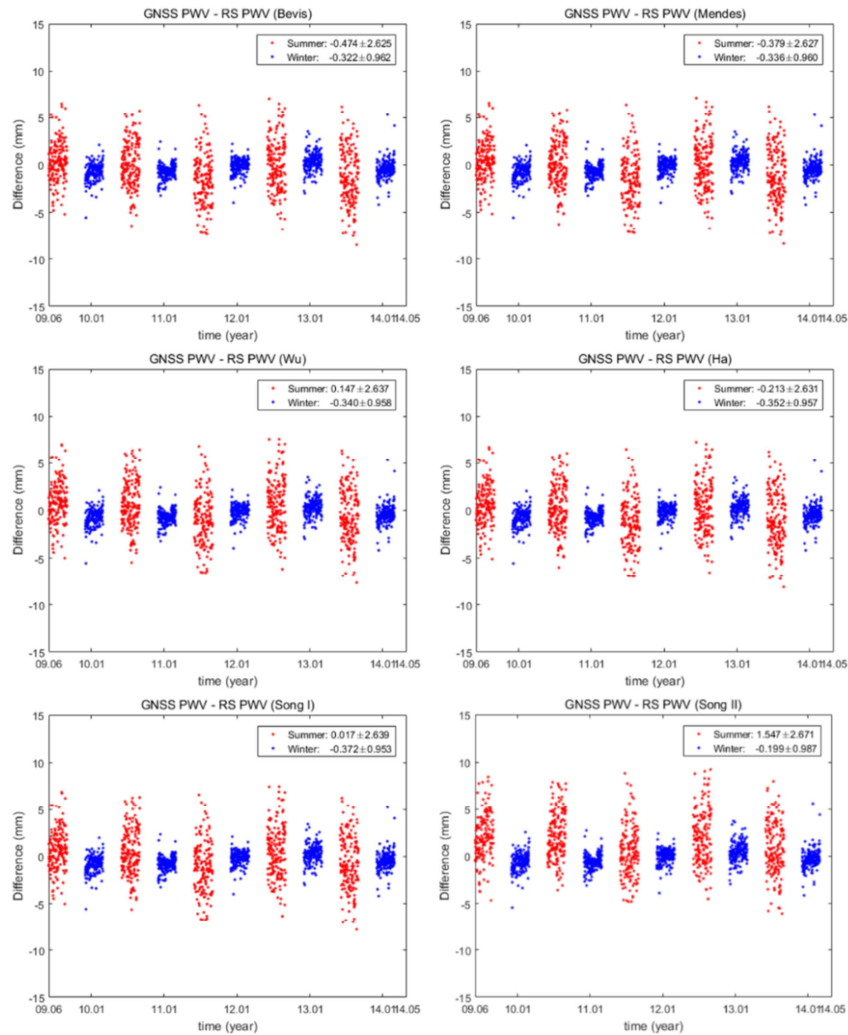
Figure 5-5. GNSS PWVs applied different mean temperature models were compared to RS particularly in summer and winter for Sokcho site from 2009 to 2014.

To check the effects of the MTE biases in summer and winter, GNSS PWV estimated from each model were compared to Radiosonde (RS) measurements during the period from 2009 to 2014 over the Sokcho (Park et al., 2016). The comparison results are shown in Figure 5-5. Although the local seasonal models, which are Song I and Song II, are best fitted to Radiosonde PWV, local annual model Wu was selected as an optimal model because boundaries of the seasons are not clear. In addition, the annual model is proper to maintain consistency of near real-time GNSS PWV.
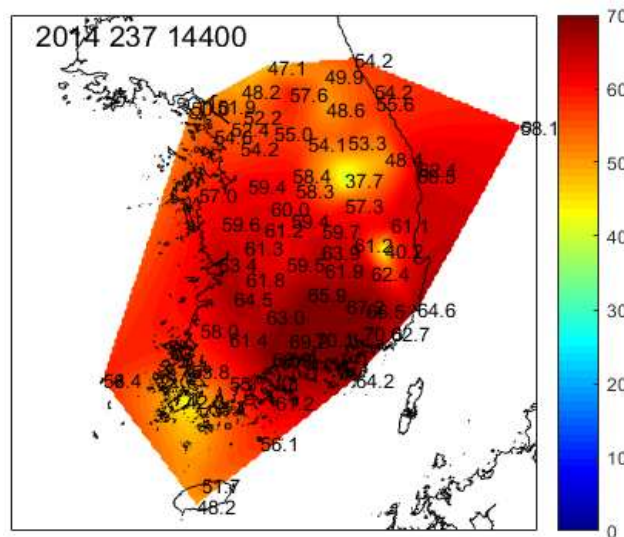
Figure 5-6. GNSS PWV for Heavy rainfall in Aug. 25, 2014.
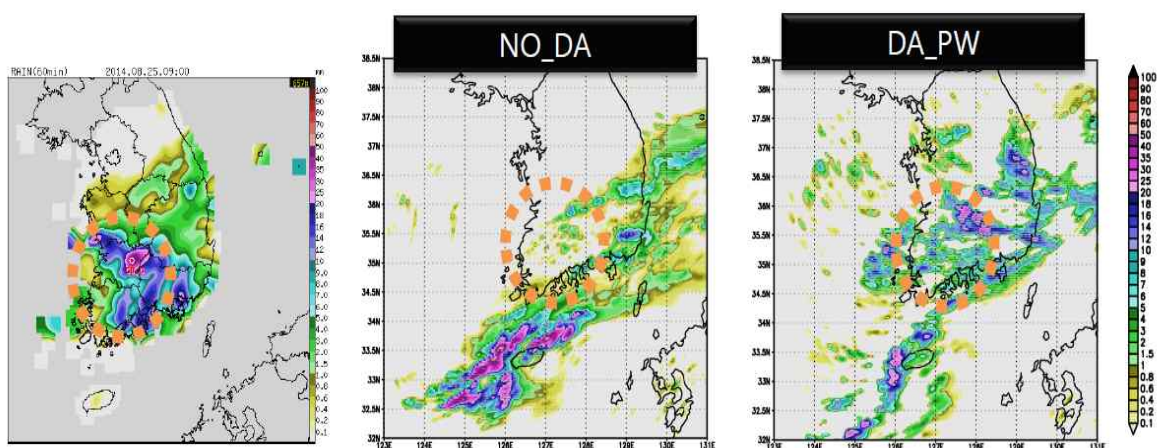
Figure 5-7. Precipitation contour map of the heavy rainfall events (left), weather forecast at that time with no the optimal GNSS PWV data assimilation (middle), and WRF prediction with 3D-Var assimilation of the optimal GNSS PWV (right).

To check the applicability of the GNSS PWV to weather forecast, a heavy rainfall event in August, 2014 was chosen. The GNSS PWV estimates based on VMF1 and Wu MTE were applied to WRF 3D-Var assimilation (KASI, 2016). Figure 5-6 shows optimal estimation of the GNSS PWV over South Korea for the event period. While weather forecast at that time failed to heavy rainfall in southwest part (dashed circles), WRF prediction including the GNSS PWV information was improved particularly in the area of dashed circles in Figure 5-7.

Ionosphere

Ionospheric Storms in Korea

The two radio frequencies (L1=1.57542 GHz and L2=1.22760 GHz) transmitted the Global Positioning System (GPS) satellites at the altitude of 20,200 km can be abnormally refracted or degraded by suddenly temporal and spatial variations of electron densities when its radio signals pass through the Earth's ionosphere. The unusually enhanced electron densities in the ionosphere make the unexpected GPS time delay errors and its irregularities can fluctuate the amplitudes and phases of GPS L1 and L2 signals called by ionospheric scintillation. These abnormal ionospheric variations finally result in the low accuracy in GPS position (Ledvina et al., 2002; Xu et al. 2007). Thus, understanding of abnormal ionospheric variations can practically help to the GPS error estimation. Here we will firstly present the results of the statistical analysis of ionospheric storms over Korea using GPS TEC measurements from the ground-based JEJU GNSS site which has been operated by KASI since 2002. This work presents statistics of positive and negative ionospheric storms using GPS TEC data observed at the KASI JEJU GNSS site between 2002 and 2014. The number of positive ionospheric storms was 170, which is more than five times the number of negative ionospheric storms of 33. The trends of both positive and negative ionospheric storms seem to follow the solar activity during solar cycle 23, but only positive ionospheric storms show the solar activity variation during solar cycle 24. The number of positive and negative storms during solar cycles 23 and 24 were 134 and 69, respectively. This result indicates that the ionosphere was actively perturbed in solar cycle 23, whereas it was relatively quiet in solar cycle 24 in Korea. Ionospheric storms frequently occurred during May to July. The occurrence of the negative

ionospheric storms shows the seasonal trend of the maximum in summer. The positive ionospheric storms show larger occurrence during solstices than equinoxes.
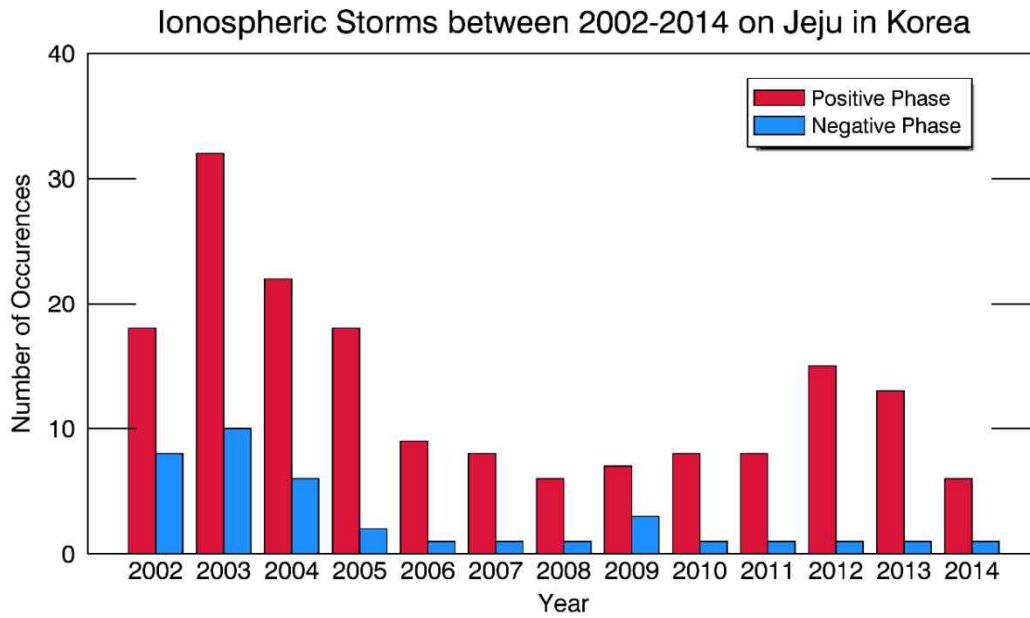
Figure 5-8. Yearly trend of ionospheric storm between 2002 and 2014 on Jeju in Korea.
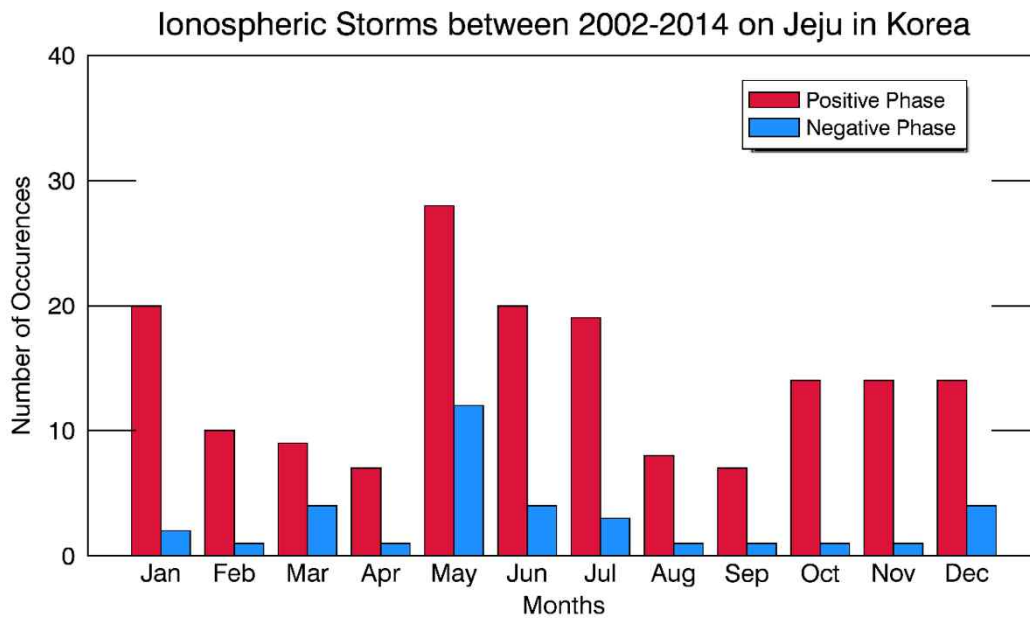
Figure 5-9. Monthly trend of ionospheric storm between 2002 and 2014 on Jeju in Korea.

Korean National Report to the International Association for Geodesy, 2019

GPS TEC variation in the equatorial region

The equatorial region of the Earth's ionosphere generally exhibits the largest spatial and temporal gradients in electron density (N_e) due to the well-known Equatorial Ionization Anomaly (EIA), with a trough at the geomagnetic equator and two crests at ~15° north and south geomagnetic latitudes. Ionospheric measurements using GPS TEC are very sparse in the East Asia Pacific region because a significant portion of the EIA is over the ocean, where ground-based receivers cannot be deployed. KASI has been operating a permanent geodetic GNSS station in the Korea South Pacific Ocean Research Center of the Korea Institute of Ocean Science and Technology (KIOST). The station is located at Chuuk (Geographic: 7.5° N, 151.9° E; Geomagnetic: 0.4° N, site marker name: CHUK) in the Federated States of Micronesia. It is the ideal location to study the ionospheric characteristics of the EIA trough that have not been thus far observed.

Daily mean TEC values exhibited the variation corresponding to the 27-day period of the solar rotation; this trend showed a clear contrast in summer. The seasonal variation of daily mean TEC exhibits the combined features together with the semi-annual anomaly, the equinoctial asymmetry, and the annual anomaly. The semi-annual anomaly had the amplitudes of 12.4 TECU (33%) on March 19 and 8.8 TECU (23%) on October 25, with a yearly average value of 38.0 TECU. An equinox asymmetry was also observed where the March equinox has higher amplitude than the October equinox, as shown by the daily mean TEC variation. The last anomaly feature reflected the annual anomaly where the daily mean TEC values were higher in December than in June.

The annual/semi-annual anomaly and equinoctial asymmetry may be explained by the significant effects of the solar flux variation between 08:00 and 18:00 LT. During daytime, the first and second peaks of the semi-annual anomaly occurred in March and October, respectively. It disappeared after midnight and began to gradually develop after 06:00 LT. The nighttime GPS TEC enhancements between 20:00 LT and 24:00 LT similarly exhibited the semi-annual variation during daytime. Considerable peaks appeared around 22:00–23:00 LT in the spring equinox, whereas the GPS TEC values continuously decreased during daytime in the autumn equinox. The nighttime TEC enhancement between 22:00− 23:00 LT in the spring equinox could be attributed to the mixed effect of the slow N_e loss time and other N_e production mechanisms such as the Pre-Reversal Enhancement during the spring equinox. The ionospheric anomaly originally indicates any departure from the solar-controlled

ionospheric behavior, and many research topics have retained its physical mechanism and effects of GPS radio signals. Ionospheric storms, which may cause degradation of GPS abilities, might develop more vigorously under ionospheric anomalies according to solar and geomagnetic activities (Mendillo 2006; Rishbeth & Müller-Wodarg 2006).
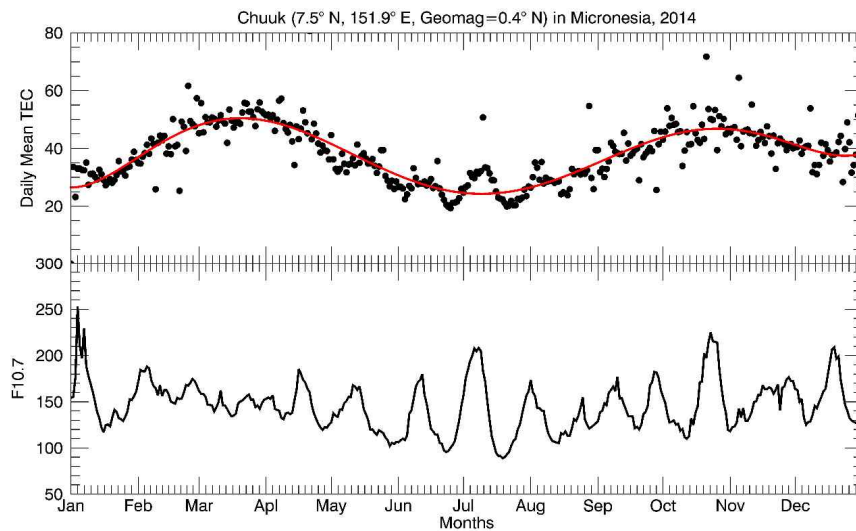
Figure 5-10. Monthly variations of the daily mean TEC values (solid circle) measured from the KASI CHUK GPS site and its fitting line (red line) and F10.7 index under quiet geomagnetic condition (Kp ≤ 3.0) in 2014
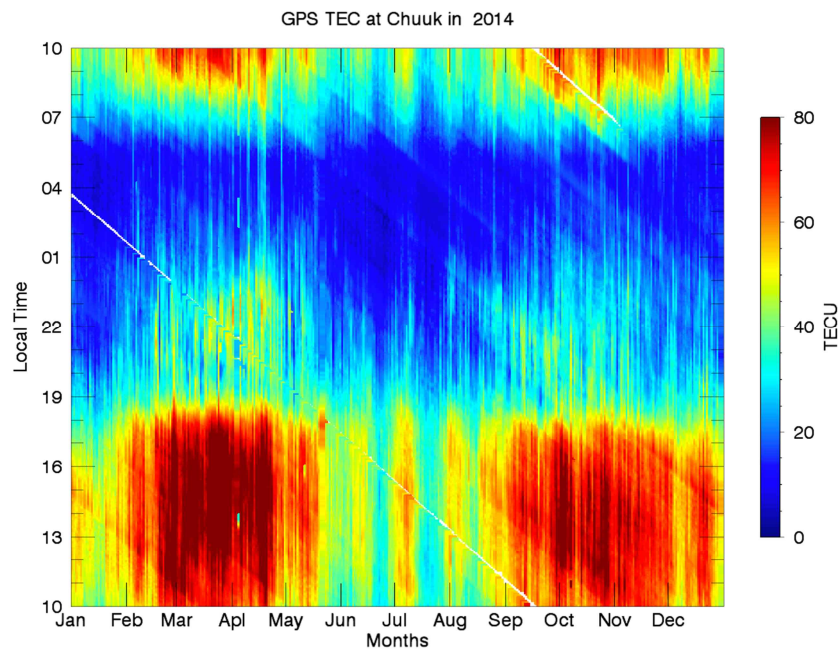
Figure 5-11. Monthly variations of the mean VTEC values with local time on the solar maximum in 2014 from the KASI CHUK GPS site

5.3 SLR Dynamics

Spin Dynamics of Artificial Satellites

At present, 182 satellites are registered with the ILRS. These satellites rely on SLR for tracking, and 141 of them have reached the end of their mission or life span. For satellites at the end of their lives, attitude control becomes difficult, and rate of rotation decreases due to forces of the Earth's gravitational and magnetic fields, torque, and solar activity. They are no longer able to maintain stable attitudes. Attitude information is required in order to precisely predict and determine satellite orbits. SLR systems enable precise measurement of rate of rotation and axis directions of manually-operated geodetic satellites. In 2014, Dr. Daniel Kucharski studied the spin period and attitude of Envisat using the SLR system at KASI. Envisat is presented in Figure 5-12.
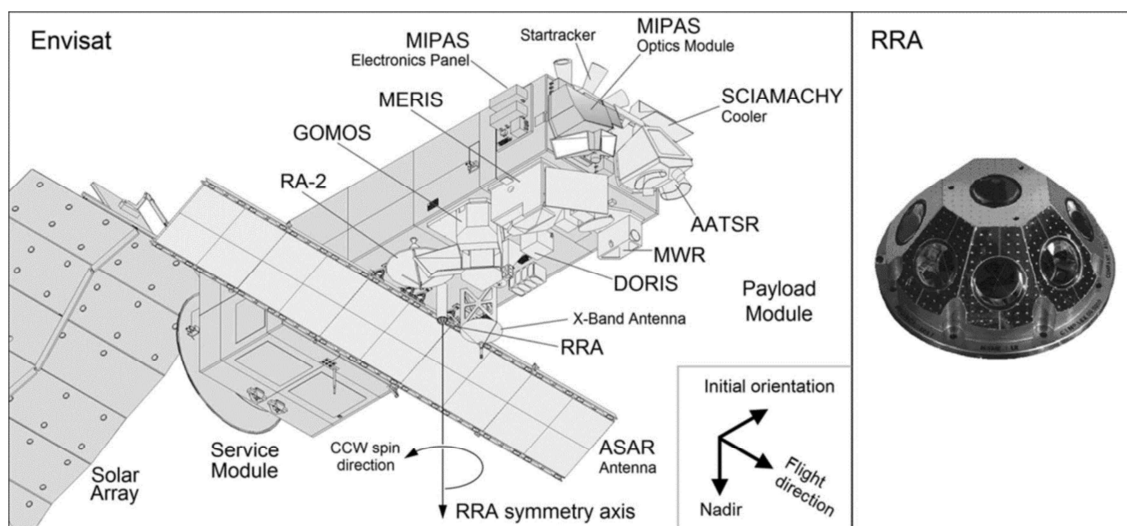
Figure 5-12. Envisat and Retro Reflector Array (RRA)

Envisat is a satellite launched into a Sun synchronous polar orbit. On April 8, 2012, its mission ended due to collision with another satellite. Upon request by ESA, Envisat was tracked using SLR for seven months beginning May 2013 to determine its rotational cycle and attitude.

Figure 5-13 shows the range residuals of Envisat as measured by the Graz SLR Station on July 12, 2013. (a) is the distribution of range residuals (average of 0), and (b) is the incident

angle between the symmetry axis of the retroreflector panel and laser vector. (c) is the amplitude function for the incident angle. Range residuals vibrate because of the offset between the retroreflector and spin axis, and the vibration period is determined by period analysis of the given data set.
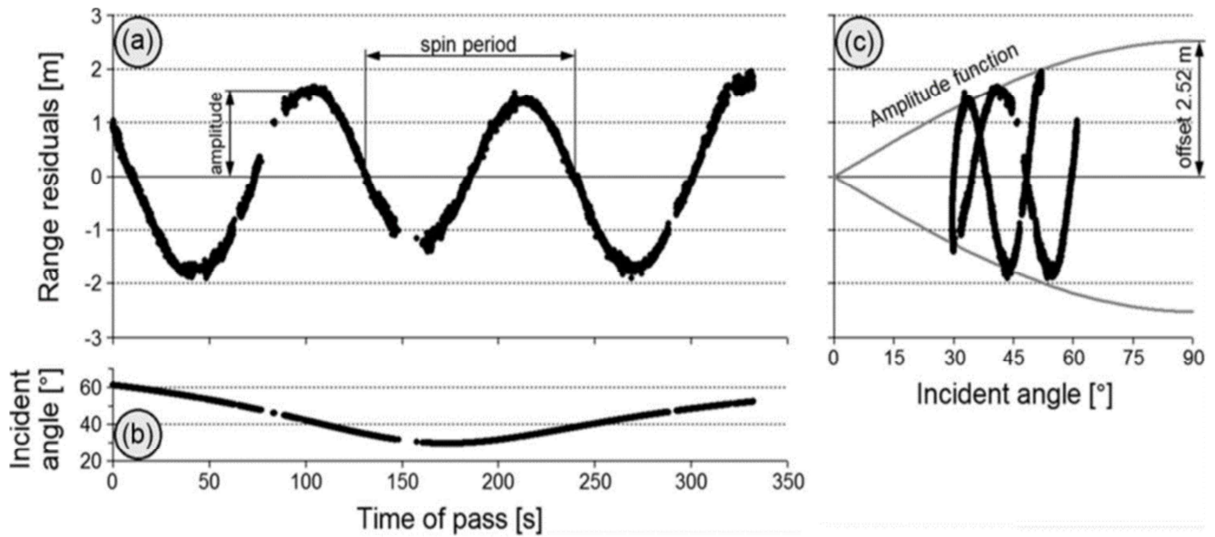
Figure 5-13. Range residuals calculated for Envisat pass measured by Graz SLR station on July 12, 2013
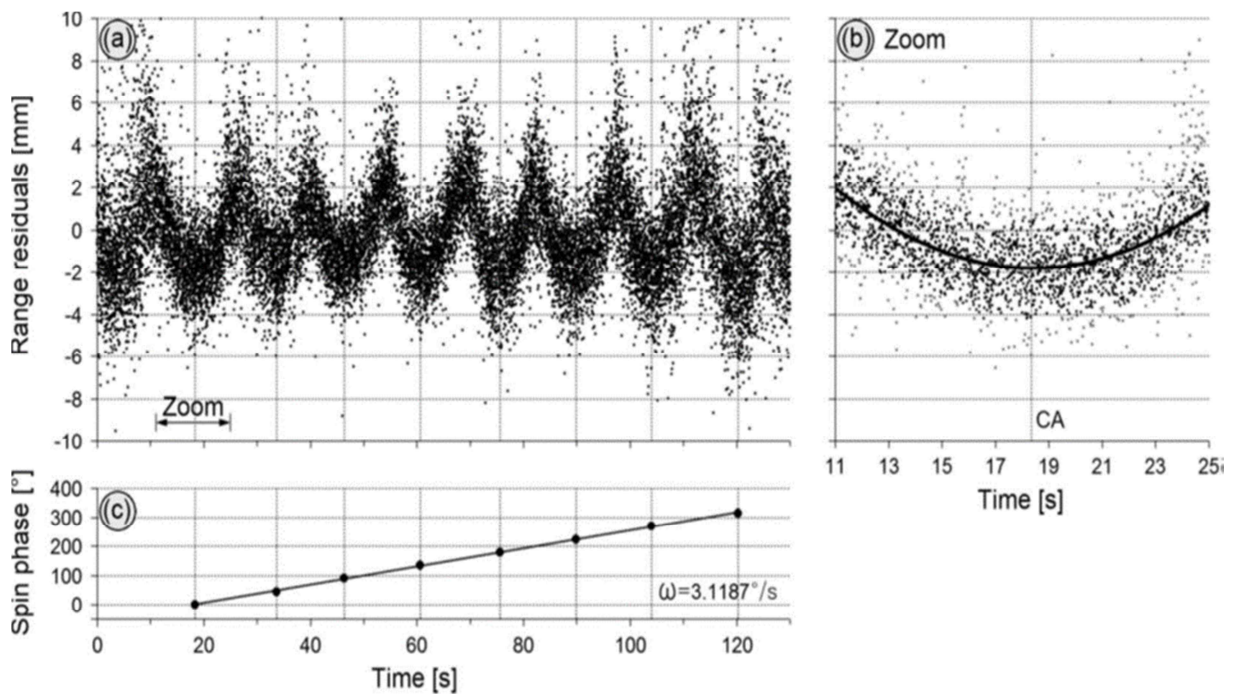
Figure 5-14. SLR data of Envisat measured by Graz on July 14, 2013

Figure 5-14 shows the SLR data measured by the Graz SLR Station on July 14, 2013, where (a) is the range residuals. The mean level is zero, and (b) is the magnification of a single CCR. The polynomial function is fitted to the accepted points (black dots). The closest approach (CA) is marked. (c) Spin phase of the satellite changes over time, i.e., the linear trend represents an apparent spin rate of the body $\omega = 3.1187$ °/s. The timescale is in seconds from the second of day = 76180. The vertical lines indicate epochs of the CA of the CCRs

INTERNATIONAL CONFERENCES

The 20th UNRCC-AP and the 4th UN-GGIM-AP

The NGII hosted the Fourth Plenary Meeting of UN-GGIM-AP in conjunction with the Twentieth United Nations Regional Cartographic Conference for Asia and the Pacific (UNRCC-AP) in Jeju from Oct. 6 to 10, 2015 under the theme 'Geospatial Information for the Global Development Agenda'. The conferences were attended by representatives from the 34 member states, and the UN-GGIM director. 6 agenda items including 'Global Positioning Standards', 'Land and Disaster Management' and 'Implementation of Regional Spatial Information', and three years' worth of activity plans were resolved for these agenda items. In conjunction with the conferences, Korea took the initiative to sign joint MOUs with four Eurasian countries, Kazakhstan, Uzbekistan, Kyrgyzstan and Mongolia. As per the MOU, conferences will be hosted for the signatories, and this is expected to accelerate the adoption of Korean advanced technologies to Eurasia. Other events held in conjunction included an exhibition hall for Korean firms, competency-training workshops, land management workshops, place name workshops, and Korea-Japan geodesy cooperation meetings, establishing the event as one of the most prestigious international geodesy conferences in the region.

Figure IC-1. Twentieth United Nations Regional Cartographic Conference for Asia and the Pacific (Delegations from 34 member states)

Figure IC-2. Land management workshop by UN ESCAP

Figure IC-3. Signing of MOU with five Eurasian countries

COSPAR Symposium 2017

The COSPAR Symposium 2017 was held in the International Convention Center (ICC) in Jeju City, Jeju Island, Korea from September 18 to 22, 2017 with the topic of "Small Satellites for Space Research". The symposium was hosted by KASI in cooperation with the Korean Space Science Society (KSSS), and supported by the Committee on Space Research (COSPAR) and Ministry of Science and ICT (Information and Communication Technology). Financial support for the symposium was provided by Korea Aerospace Research Institute (KARI), Satrec Initiative, Japan Aerospace Exploration Agency (JAXA), Asian office of Aerospace Research Development, GOM Space, Korea Polar Research Institute (KOPRI), Korea Federation of Science and Technology Societies (KOFST), Korea Tourism Organization (KTO), and Jeju Special Self-Governing Province. The total number of submitted, accepted, and presented papers was 371, 348, and 232, respectively, and the total number of participants was 361 from 37 countries. On the first day of the symposium, a Space Agency Round Table took place with the theme of "National Strategy Plans for Small Satellites". This program is designed to strengthen the communication and technical ties

between the space agencies. Two keynote speeches and twelve plenary talks were also presented.

Figure IC-4. The 3ʳᵈ COSPAR Symposium (http://www.cospar2017.org/)

PUBLICATION LISTS

Reports

Korea Astronomy and Space Science Institute (2015) Development of GNSS PWV and TEC information management system for the Earth change analysis (2nd year), *Report to Korea Institute of Science and Technology Information.*

Korea Astronomy and Space Science Institute (2016) Development of GNSS PWV and TEC information management system for the Earth change analysis (3rd year), *Report to Korea Institute of Science and Technology Information.*

Korea Astronomy and Space Science Institute (2017) Development of GNSS PWV and TEC information management system for the Earth change analysis (4th year), *Report to Korea Institute of Science and Technology Information.*

Korea Astronomy and Space Science Institute (2018) Operation and Research for Satellite Laser Ranging System.

Korea Astronomy and Space Science Institute (2018) Operation of Space Geodetic Infra-facilities and Research on Astronomical Almanac.

National Geographic Information Institute (2018) Development of the 2017 Geoid model and the Transformation model of land - maritime height.

National Geographic Information Institute (2018) Time Series Analysis of VLBI Data with TDA and deep learnings

Korean National Report to the International Association for Geodesy, 2019

Reviewed Papers

2015

Choi, B.-K., C.-H. Cho, and J. Cho (2015) Evaluation of Point Positioning Using the Global Positioning System and the Quasi-Zenith Satellite System as Measured from South Korea, *Journal of Astronomy and Space Sciences*, **32(4)**, 403-409.

Choi, B.-K., C.-H. Cho, J. Cho, and S. J. Lee (2015) Multi-GNSS Standard Point Positioning using GPS, GLONASS, BeiDou and QZSS Measurements Recorded at MKPO Reference Station in South Korea, *Journal of Positioning, Navigation, and Timing*, **4(4)**, 205-211.

Choi, B.-K., C.-H. Cho, and S. J. Lee (2015) Precise Point Positioning using the BeiDou Navigation Satellite System in South Korea, *Journal of Positioning, Navigation, and Timing*, **4(2)**, 73-77.

Choi, J., J. H. Jo, K.-M. Roh, J.-Y. Son, M.-J. Kim, Y.-J. Choi, H.-S. Yim, H.-K. Moon, B.-Y. Kim, J.-H. Park, and E. C. Pavlis (2015) Analysis of the angle-only orbit determination for optical tracking strategy of Korea GEO satellite, COMS, *Advances in Space Research*, **56(6)**, 1056-1066.

Chung, J.-K., and B.-K. Choi (2015) Statistics of Ionospheric Storms Using GPS TEC Measurements Between 2002 and 2014 in Jeju, Korea, *Journal of Astronomy and Space Sciences*, **32(4)**, 335-340.

Kil, H., Y.-S. Kwak, W. K. Lee, J. Krall, J. D. Huba, and S.-J. Oh (2015) Non-migrating tidal signature in the distributions of equatorial plasma bubbles and prereversal enhancement, *Journal of Geophysical Research: Space Physics*, **120(4)**, 3254-3262.

Kil, H., Y.-S. Kwak, W. K. Lee, E. S. Miller, S.-J. Oh, and H.-S. Choi (2015) The causal relationship between plasma bubbles and blobs in the low latitu de F region during a solar minimum, *Journal of Geophysical Research: Space Physics*, **120(5)**, 3961-3969.

Lee, K., H. Oh, H.-E. Park, S.-Y. Park, C. Park (2015) Laser-based Relative Navigation Using GPS Measurements for Spacecraft Formation Flying, *Journal of Astronomy and Space Sciences*, **32(4)**, 387-393.

Lee, W. K., H. Kil, Y.-S. Kwak, and L. J. Paxton (2015) Morphology of the postsunset vortex in the equatorial ionospheric plasma drift, *Geophysical Research Letters*, **42(1)**, 9-14.

Na, S. and J. Cho (2015) Effects of Earth's Atmosphere on Terrestrial Reference Frame: A Review, *Geophysics and Geophysical Exploration*, Vol. 18, No. 3, p. 133-142.

Yang, T. Y., Y. S. Kwak, H. Kil, Y. S. Lee, W. K. Lee, and J. J. Lee (2015) Occurrence climatology of F region field aligned irregularities in middle latitudes as observed by a 40.8 MHz coherent scatter radar in Daejeon, South Korea, *Journal of Geophysical Research: Space Physics*, **120(11)**, 10107-10115.

2016

Choi, B.-K., and S. J. Lee (2016) Anomalous ionospheric disturbances over South Korea prior to the 2011 Tohoku earthquake, *Advances in Space Research*, **57(1)**, 302-308.

Choi, B.-K., S. J. Lee, and H. S. Yoon (2016) Ionospheric TEC Disturbances over South Korea Following the 2011 Great Tohoku Earthquake, *Research Invent: International Journal of Engineering and Science*, **6(6)**, 35-42.

Choi, M., Lim, H., Lee, S., (2016) "Development and Preliminary Performance Analysis of a fast and high precision Tracking Mount for 1m Satellite Laser Ranging", J. of the Korean Society for Aeronautical and Space Sciences Vol.44(11), pp1006-1015.

Chung, J.-K., S.-M. Yoo, and W. K. Lee (2016) The First Measurement of Seasonal Trends in the Equatorial Ionospheric Anomaly Trough at the CHUK GNSS Site during the Solar Maximum in 2014, *Journal of Astronomy and Space Sciences*, **33(4)**, 287-293.

Kil, H., W. K. Lee, L. J. Paxton, M. R. Hairston, and G. Jee (2016) Equatorial broad plasma depletions associated with the evening prereversal enhancement and plasma bubbles during the 17 March 2015 storm, *Journal of Geophysical Research: Space Physics*, **121**, 10209-10219.

Kim, D., H. S. Yoon, J. Kim, and Y. Choi (2016) Evaluating accuracy of tidal datum level using spatial interpolation, *Spatial Information Research*, **24(6)**, 709-718.

Kim, Y., Park, E., Daniel, K., et al., (2016) "The challenge of precise orbit determination for STSAT-2C using extremely sparse SLR data", Advances in Space Research Vol.57, pp1159-1176.

Na, S.-H., J. Cho, T.-H. Kim, K. Seo, K. Youm, S.-M. Yoo, B.-K. Choi, and H. Yoon (2016) Changes in the Earth's Spin Rotation due to the Atmospheric Effects and Reduction in Glaciers, *Journal of Astronomy and Space Sciences*, **33(4)**, 247-256.

Oh, H., H.-E. Park, K. Lee, S.-Y. Park, C. Park (2016) Improved GPS-based Satellite Relative Navigation Using Femtosecond Laser Relative Distance Measurements, *Journal of Astronomy and Space Sciences*, **33(1)**, 45-54.

Park, C.-G., J. Cho, J.-K. Shim, and B.-C. Choi (2016) Analysis on characteristics of Radiosonde sensors bias using PWV from Sokcho GNSS Obs., *Korean Journal of Remote Sensing*, **32(3)**, 263-274.

Park, H.-E., and Y.-R. Kim (2016) Relative navigation for autonomous formation flying satellites using the state-dependent Riccati equation filter, *Advances in Space Research*, **57(1)**, 166-182.

Park, H.-E., S.-M. Yoo, H. S. Yoon, J.-K. Chung, and J. Cho (2016) Performance Analysis of Mapping Functions and Mean Temperature Equations for GNSS Precipitable Water Vapor in the Korean Peninsula, *Journal of Positioning, Navigation, and Timing*, **5(2)**, 75-85.

Roh, K.-M., S. M. Kopeikin, and J.-H. Cho (2016) Numerical simulation of the post-Newtonian equations of motion for the near Earth satellite with an application to the LARES satellite, *Advances in Space Research*, **58**, 2255-2268.

Yoon, H. S., Y. S. Choi, and J. H. Kwon (2016) Accuracy Analysis of Ocean Tide Loading Constituent Detection Using GNSS Positioning, *Journal of the Korean Society of Surveying, Geodesy, Photogrammetry and Cartography*, **34(3)**, 299-308.

2017

Cho, C.-H., and B.-K. Choi (2017) A Periodic Analysis of Sidereal Shifts for GPS Satellites and the Solar Wind Stream, *Journal of Positioning, Navigation, and Timing*, **6(2)**, 71-78.

Choi, B.-K., C.-H. Cho, and S. J. Lee (2017) Multi-GNSS Kinematic Precise Point Positioning: Some Results in South Korea, *Journal of Positioning, Navigation, and Timing*, **6(1)**, 35-41.

Choi, B.-K., and H. Kil (2017) Large ionospheric TEC depletion induced by the 2016 North Korea rocket, *Advances in Space Research*, **59**, 532-541.

Choi, B.-K., H. S. Yoon, and S. J. Lee (2017) Positioning Precision Improvement of Multi-GNSS Kinematic PPP Using WMN Method, *Journal of Positioning, Navigation, and Timing*, **6(4)**, 203-208.

Choi, J.-M., H. Kil, Y.-S. Kwak, J. Park, W. K. Lee, and Y. H. Kim (2017) Periodicity in the occurrence of equatorial plasma bubbles derived from the C/NOFS observations in 2008-2012, *Journal of Geophysical Research: Space Physics*, **122(1)**, 1137-1145.

Chung, J.-K., J. Hong, S.-M. Yoo, J.-H. Kim, G. Jee, and V. V. Hegai (2017) GPS TEC Fluctuations in the Low and High Latitudes During the 2015 St. Patrick's Day Storm, *Journal of Astronomy and Space Sciences*, **34(4)**, 245-250.

Hong, J., Y. H. Kim, J.-K. Chung, N. Ssessanga, and Y.-S. Kwak (2017) Tomography Reconstruction of Ionospheric Electron Density with Empirical Orthonormal Functions Using Korea GNSS Network, *Journal of Astronomy and Space Sciences*, **34(1)**, 7-17.

Kim, V. P., V. V. Hegai, J. Y. Liu, K. Ryu, and J.-K. Chung (2017) Time-Varying Seismogenic Coulomb Electric Fields as a Probable Source for Pre-Earthquake Variation in the Ionospheric F2-Layer, *Journal of Astronomy and Space Sciences*, **34(4)**, 251-256.

Liu, H., J. Thayer, Y. Zhang, and W. K. Lee (2017), The non-storm time corrugated upper thermosphere: What is beyond MSIS?, *Space Weather*, **15(6)**, 746-760.

Park, J., H. Luehr, G. Kervalishvili, J. Rauberg, C. Stolle, Y.-S. Kwak, and W. K. Lee (2017) Morphology of high-latitude plasma density perturbations as deduced from the total electron content measurements onboard the Swarm constellation, *Journal of Geophysical Research: Space Physics*, **122(1)**, 1338-1359.

Yoon, H. S., J. Cho, H. E. Park, and S. M. Yoo (2017) Development of Near Real Time GNSS Precipitable Water Vapor System Using Precise Point Positioning, *Journal of the Korean Society of Surveying, Geodesy, Photogrammetry and Cartography*, **35(6)**, 471-484.

2018

Choi, B.-K., and S. J. Lee (2018) The influence of grounding on GPS receiver differential code biases, *Advances in Space Research*, **62(2)**, 457-463.

Choi, B.-K., and H. S. Yoon (2018) Positioning stability improvement with inter-system biases on multi-GNSS PPP, *Journal of Applied Geodesy*, **12(3)**, 239-248.

Choi, B.-K., H. S. Yoon, and S. J. Lee (2018) Combined GPS/GLONASS Relative Receiver DCB Estimation Using the LSQ Method and Ionospheric TEC Changes over South Korea, *Journal of Positioning, Navigation, and Timing*, **7(3)**, 175-181.

Choi, J., J. H. Jo, K.-M. Roh, H.-S. Yim, E.-J. Choi, and S. Cho (2018) Characteristics of Orbit Determination with Short-Arc Observation by an Optical Tracking Network, OWL-Net, *International Journal of Aerospace Engineering*, **2018**, 1-11.

Kim, S., J.-H. Ree, H. S. Yoon, B.-K. Choi, and P.-H. Park (2018) Crustal Deformation of South Korea After the Tohoku-Oki Earthquake: Deformation Heterogeneity and Seismic Activity, *Tectonics*, **37**, 2389-2403.

Lee, J., I. Park, J. Cho, G. D. Ki, and Y. C. Kim (2018) Development of a Prototype Device to Capture Day/Night Cloud Images based on Whole-Sky Camera using the Illumination Data, *Atmosphere, Korea Meteological Society*, **28(3)**, 317-324.

Lee, W. K., H. Kil, and L. J. Paxton (2018) Tropical Ionization Trough in the Ionosphere Seen by Swarm-A Satellite, *Geophysical Research Letters*, **45(22)**, 12135-12141.

Lim, H., Sung, K., Yu, S., et al., (2018) "Satellite Laser Ranging System at Geochang Station", J. of the Korean Space Science Society Vol.35(4), pp253-261.

Na, S., J. Cho, K.W. Seo, K.H. Youm, and W. Shen (2018) A note on the annual wobble excitation due to the seasonal atmospheric loading on continents, *Terr. Atmos. Ocean. Sci.*, Vol. 29, No.6, p. 721-729.

Roh, K.-M. (2018) Numerical Evaluation of Post-Newtonian Perturbations on the Global Navigation Satellite System, *Journal of Spacecraft and Rockets*, **55(4)**, 1027-1032.

Ssessanga, N., Y. H. Kim, B. Choi, and J.-K. Chung (2018) The 4D-var Estimation of North Korean Rocket Exhaust Emissions into the Ionosphere, *Journal of Geophysical Research: Space Physics*, **123(3)**, 2315-2326.

Yoo, S.-M., T. Jung, S.-M. Lee, H. S. Yoon, H.-E. Park, J.-K. Chung, K.-M. Roh, S. O. Wi, J. Cho, and D.-Y. Byun (2018) Determination of the invariant point of the Korean VLBI network radio telescopes: First results at the Ulsan and Tamna observatories, *Journal of the Korean Astronomical Society*, **51**, 143-153.

2019

Choi, B.-K., and J. Hong (2019) Observation of the fast-traveling ionospheric disturbances induced by the 2017 North Korean missile, *Advances in Space Research*, **63(8)**, 2598-2608.

Na, S.-H., K.-M. Roh, J. Cho, S.-M. Yoo, B. Choi, and H. Yoon (2019) Chandler Wobble and Free Core Nutation: Theory and Features, *Journal of Astronomy and Space Sciences*, **36(1)**, 11-20.

Na, S.-H., W. Shen, J. Cho, K. Seo, Y.-H. Shin, K.-D. Park, K. Youm, and S.-M. Yoo (2019) Earth rotation deceleration/acceleration due to semidiurnal oceanic/atmospheric tides: Revisited with new calculation, *Geodesy and Geodynamics*, **10**, 37-41.

REFERENCES

2. Space Geodetic Infrastructure

S.-M. Yoo, T. Jung, S.-M Lee, H. Yoon, H.-E. Park, J.-K. Chung, K.-M. Roh, S. Wi, J. Cho, and D.-Y. Byun (2018) Determination of the invariant point of the Korean VLBI network radio telescopes: First results at the Ulsan and Tamna observatories, *Journal of the Korean Astronomical Society*, **51**, 143-153.

3. Gravity Field

National Geographic Information Institute (2018) Development of the 2017 Geoid model and the Transformation model of land - maritime height.

4. Earth Rotation & Geodynamics

National Geographic Information Institute (2018) Time Series Analysis of VLBI Data with TDA and deep learnings

Bizouard C. and D. Gambis (2009) The combined solution C04 for Earth orientation parameters consistent with international terrestrial reference frame 2005, *International Association of Geodesy Symposia*, Vol. 134, Geodetic Reference Frames, ed. H. Drewes, Springer, Heidelberg, pp. 265-270.

Guo, J.Y., Y.B. Li, Y. Hwang, H.T. Deng, S.Q. Xu, and J.S. Ning (2004) Green's function of the deformation of the Earth as a result of atmospheric loading, *Geophys. J. Int.*, Vol. 159, pp. 53-68.

Lambeck, K. (1980) The Earth's Variable Rotation: Geophysical Causes and Consequences, *Cambridge University Press*, pp. 10-11.

Mathews, P.M. and S.B. Lambert (2009) Effect of mantle and ocean tides on the Earth's rotation rate, *Astron. Astrophys*. 493, pp. 325-330

Munk, W.H. and G.J.F. McDonald (1960) The Rotation of the Earth, *Cambridge University Press*, Ch.11 and Ch. 4.

Na, S. and J. Baek (2011) Computation of the Load Love Number and the Load Green's Function for an Elastic and Spherically Symmetric Earth, *Journal of the Korean Physical Society*, Vol. 58, p. 1195-1205, doi:10.3938/jkps.58.1195.

Na, S. and J. Cho (2015) Effects of Earth's Atmosphere on Terrestrial Reference Frame: A Review, *Geophysics and Geophysical Exploration*, Vol. 18, No. 3, p. 133-142.

Na, S., J. Cho, T.H. Kim, K.W. Seo, K.H. Youm, S.M. Yoo, B.K. Choi, and H. Yoon (2016) Changes in the Earth's Spin Rotation due to the Atmospheric Effects and Reduction in Glaciers, *Journal of Astronomy and Space Science*, Vol. 33, No.4, pp. 247-256.

Na, S., J. Cho, K.W. Seo, K.H. Youm, and W. Shen (2018) A note on the annual wobble excitation due to the seasonal atmospheric loading on continents, *Terr. Atmos. Ocean. Sci.*, Vol. 29, No.6, p. 721-729.

Na, S., W. Shen, J. Cho, K.W. Seo, Y.H. Shin, K.D. Park, K.H. Youm, and S.M. Yoo (2019) Earth rotation deceleration/acceleration due to semidiurnal oceanic/atmospheric tides: Revisited with new calculation, *Geodesy and Geodynamics*, Vol. 10, pp. 37-41.

Ray, R.D., B.G. Bills, and B.F. Chao (1999) Lunar and solar torques on the ocean tides, *J. Geophys. Res.*, 104, pp. 17653-17659.

Ray, R.D. and R.M. Ponte (2003) Barometric tides from ECMWF operational analysis, Ann. Geophys., 23, pp. 1897-1910

Schindelegger, M. (2014) Atmophere-induced short period variations of Earth rotation, TU Wien Geowissenschaftliche Mitteillungen Heft Nr. 96.

Van Dam, T.M., Z. Altamimi, X, Collilieux, and J. Ray (2010) Topographically induced

height errors in predicted atmospheric loading effects, *Journal of Geophysical Research*, 115, B07415, doi:10.1029/2009/JB006810.

5. Applications

Korea Astronomy and Space Science Institute (2016) Development of GNSS PWV and TEC information management system for the Earth change analysis (3rd year)*, Report to Korea Institute of Science and Technology Information.*

Bevis, M., S. Businger, , T. Herring, C. Rocken, R. A, Anthes (1992) GPS meteorology: remote sensing of atmospheric water vapor using the global positioning system, *JGR*, **97**, 15787-15801

Ha, J.-H. & K.-D. Park (2008) Comparison of Local Mean Temperature Equations for GPS-based Precipitable Water Vapor Determination, *JASS,* **25**, 425-434.

Kucharski, D., K. Georg, and K. Franz (2014) Attitude and Spin Period of Space Debris Envisat Measured by Satellite Laser Ranging, *IEEE Transactions on Geoscience and Remote Sensing,* **52(12)**, pp7651-7657.

Ledvina, B. M., J. J. Maakela, and P. M. Kintner (2002) First observations of intense GPS L1 amplitude scintillations at midlatitude, *GRL*, **29**, 1659

Mendes, V. B. (1999) Modeling the neutral-atmospheric propagation delay in radiometric space techniques, *UNB Geodesy and Geomatics Engineering Technical Report*, No.199.

Mendillo, M. (2006) Storms in the ionosphere: patterns and processes for total electron content, *Rev. Geophys*., **44**, RG4001

Park, H.-E., S.-M. Yoo, H. S. Yoon, J.-K. Chung, and J. Cho (2016) Performance Analysis of Mapping Functions and Mean Temperature Equations for GNSS Precipitable Water Vapor in the Korean Peninsula, *Journal of Positioning, Navigation, and Timing*, **5(2)**, 75-85.

Rishbeth, H. and I. C. Müller-Wodarg (2006) Why is there more ionosphere in January than in July? The annual asymmetry in the F2-layer, *Ann. Geophys*., **24**, 3293-3311

Song, D.-S. and D. A. Grejner-Brzezinska (2009) Remote sensing of atmospheric water variation from GPS measurements during a severe weather event, *EPS*, **61**, 1117-1125.

Song, D. S. (2009) GPS water vapor estimation modeling with high accuracy by consideration of seasonal characteristics on Korea, *Journal of the Korean Society of Surveying, Geodesy, Photogrammetry and Cartography*, **27**, 565-574

Wu, S. (2003) Adjustment of meteorological variables for the accurate estimation of GPS PWV, Master's Degree, Seoul University, South Korea

Xu, J. S., J. Zhu, and L. Li (2007) Effects of a major storm on GPS amplitude scintillations and phase fluctuations at Wuhan in China, *Adv. Space Res*., **39**, 1318-1324

International Conferences

2017 Annual Report (2018) Korea Astronomy and Space Science Institute, pp. 23-24.